Please cite this article in press as: Fischer-Friedrich et al., Rheology of the Active Cell Cortex in Mitosis, Biophysical Journal (2016), http://dx.doi.org/10.1016/j.bpj.2016.06.008

Biophysical *Journal*
Article

Biophysical Society

Rheology of the Active Cell Cortex in Mitosis

Elisabeth Fischer-Friedrich,[1,2] Yusuke Toyoda,[1,3] Cedric J. Cattin,[4] Daniel J. Müller,[4] Anthony A. Hyman,[1,*] and Frank Jülicher[2,*]

[1]Max Planck Institute of Molecular Cell Biology and Genetics, Dresden, Germany; [2]Max Planck Institute for the Physics of Complex Systems, Dresden, Germany; [3]Institute of Life Science, Kurume University, Kurume, Japan; and [4]Department of Biosystems Science and Engineering, Eidgenössische Technische Hochschule Zürich, Basel, Switzerland

ABSTRACT The cell cortex is a key structure for the regulation of cell shape and tissue organization. To reach a better understanding of the mechanics and dynamics of the cortex, we study here HeLa cells in mitosis as a simple model system. In our assay, cells are dynamically compressed between two parallel plates. Our measurements indicate that the cortical layer is the dominant mechanical element in mitosis as opposed to the cytoplasmic interior. To characterize the time-dependent rheological response, we extract a complex elastic modulus that characterizes the resistance of the cortex against area dilation. In this way, we present a rheological characterization of the cortical actomyosin network in the linear regime. Furthermore, we investigate the influence of actin cross linkers and the impact of active prestress on rheological behavior. Notably, we find that cell mechanics values in mitosis are captured by a simple rheological model characterized by a single timescale on the order of 10 s, which marks the onset of fluidity in the system.

INTRODUCTION

The cell cortex plays a key role in determining cell mechanics, cell shape, and tissue organization (1). The cortical layer is an actin-based filament network linked to the plasma membrane (2). It is dynamically maintained at a thickness that has been estimated to range from 0.05 to 1 μm (2). Many actin-associated proteins organize the network structure and filament length including passive cross linkers and active elements such as myosin motors (2). The cortex is therefore an active material and is mechanically characterized by the cortical tension. This cortical tension results from active contractile stress generated in the cytoskeletal network by motor proteins and filament dynamics (1,2). The cortex provides a cell with an effective surface tension (2). In contrast to the surface tension of a passive system (3), such as a liquid drop, cell surface tension can be locally regulated by cellular signaling processes (1,4). This allows the cell to use cortical mechanics to regulate shape and, together with cell adhesion, to guide tissue organization (1). For example, cortical tension can regulate cell shape in a tissue, and drive tissue remodeling processes such as T1 transitions (5,6) and cell extrusions from an epithelium (7). During mitosis, increasing cell surface tension leads to cell rounding. In this way, cells provide sufficient space for the formation of a mitotic spindle unhindered by complex cell geometry found in tissues (8). Cell rounding is associated with major remodeling of the actomyosin cytoskeleton and an increase in cortical tension that is accompanied by a corresponding increase of hydrostatic pressure (9–11). Round cells will then divide into two during cytokinesis, and return to interphase.

While there is extensive work on the mechanics of the interphase cortex, we know much less about the mechanics of the mitotic cortex. Therefore, we do not understand how mechanical properties of the cortex change to prepare cells for division. Recently, using a parallel plate assay (12), we have shown that compressed mitotic cells acquire a well-defined shape of minimal surface area (10). This permits tight control of cell geometry during measurements of strain and steady-state active tension. Here, by measuring these quantities, we show that cell mechanics in mitosis is dominated by the cortical layer of the cell. Because we can distinguish the cortex from the cytoplasm, this allows us to measure the time-dependent mechanical response of the cortical layer in vivo.

MATERIALS AND METHODS

Cell culture

We cultured HeLa Kyoto cells expressing a fluorescent histone construct (H2B-GFP) in DMEM supplemented with 10% (vol/vol) fetal bovine serum, 2 mM GlutaMAX, 100 μg/mL penicillin, 100 μg/mL streptomycin,

Submitted November 2, 2015, and accepted for publication June 9, 2016.

*Correspondence: hyman@mpi-cbg.de or julicher@pks.mpg.de

Editor: Cecile Sykes.

http://dx.doi.org/10.1016/j.bpj.2016.06.008

Please cite this article in press as: Fischer-Friedrich et al., Rheology of the Active Cell Cortex in Mitosis, Biophysical Journal (2016), http://dx.doi.org/10.1016/j.bpj.2016.06.008

and 0.5 μg/mL geneticin (all Invitrogen, Carlsbad, CA) at 37°C with 5% CO_2. One day before the measurement, 10,000 cells were seeded into a silicon cultivation chamber (0.56 cm^2, from a 12-well chamber; Ibidi, Martinsried, Germany) that was placed in a 35-mm cell culture dish (glass bottom Fluorodish FD35-100; World Precision Instruments, Sarasota, FL) such that a confluency of $\approx$30% is reached at the day of measurement. For atomic force microscopy (AFM) experiments, medium was changed to DMEM (Cat. No. 12800-017; Invitrogen) with 4 mM $NaHCO_3$ buffered with 20 mM HEPES/NaOH at pH 7.2. Where indicated, mitotic cells were detached from cell culture dishes with Trypsin/EDTA and measured on dishes coated with PLL-g-PEG (SuSoS, Dubendorf, Switzerland) that prevents cell adhesion but does not induce significant changes in cell surface tension (13). For PEG-coating, dishes were first plasma-cleaned and then incubated for $\approx$30 min in 0.1 mg/mL PLL-g-PEG solution and afterwards rinsed with PBS and used up to 24 h afterwards. We used the cytoskeletal drugs blebbistatin (Cat. No. B0560; Sigma-Aldrich, St. Louis, MO), latrunculin A (Cat. no. 428021; Merck, www.merck.com), taxol (Cat. No. T7191; Sigma-Aldrich), or nocodazol (Cat. No. M1404; Sigma-Aldrich), where indicated. Drugs were added to indicated concentrations at least 10 min before the experiment. Mitotic arrest of cells was achieved by addition of S-trityl-L-cysteine (STC; Sigma-Aldrich) 2–8 h before the experiment at a concentration of 2 μM. This allowed conservation of cell mechanical properties during measurement times of up to 30 min for one cell (14). Cells in mitotic arrest were identified by their shape and/or H2B-GFP. Diameters of uncompressed, roundish, mitotic cells typically ranged from 19 to 23 μm. We verified that mechanical properties of cells in mitotic arrest are similar to those of cells in metaphase of mitosis (Fig. S16 in the Supporting Material).

Atomic force microscopy

The experimental setup consisted of an atomic force microscope (Nanowizard I; JPK Instruments, Berlin, Germany) mounted on an Axiovert 200M optical, wide-field microscope (Carl Zeiss, Jena, Germany). For imaging, we used a 20× objective (Plan Apochromat, NA = 0.80; Carl Zeiss) and an AxioCam charge-coupled device camera (Carl Zeiss). During measurements, cell culture dishes were kept in a petri dish heater (JPK Instruments) at 37°C. On every measurement day, the spring constant of the cantilever was calibrated using the thermal noise analysis (built-in software; JPK Instruments). Cantilevers were tipless, 200–350-μm long, 35-μm wide, 2-μm thick, and made of pure silicon (NSC12/tipless/noAl or CSC37/tipless/noAl, from MikroMasch; www.mikromasch.com) with nominal force constants between 0.3 and 0.8 N/m. Cantilevers were modified in either of two ways to correct for the 10° cantilever tilt and allow for axisymmetric confinement. For this purpose, cantilevers were supplemented by wedges consisting of UV-curing adhesive (Norland Optical Adhesive 63; Norland Products, Cranbury, NJ) (12). During measurements, measured force, piezo height, and time were output at a time resolution of 10 Hz (compression steps) or 100 Hz (oscillatory compressions). For AFM compression of detached mitotic cells on PEG-coated dishes, we used the CellHesion module (JPK Instruments), which allowed us to vertically control the AFM cantilever in a 100-μm range (15).

Progressive uniaxial compression of cells

To probe the viscoelastic response of cells, we progressively compressed them with the AFM cantilever. Before cell compression, the AFM cantilever was lowered to the dish bottom near the cell until it came into contact with the surface and then retracted to $\approx$15 μm above the surface. Thereafter, the free cantilever was moved over the cell. The cantilever was then gradually lowered in steps of 0.5–1 μm at a set speed of 0.5 μm/s interrupted by waiting times of 60–100 s. During these waiting times, the AFM cantilever was held at constant height and the measured force was relaxing. The force acting on the cantilever was continuously recorded. The height of the confined cell was computed as the difference between the height that the cantilever was raised from the dish surface and lowered onto the cell plus the height of spikes at the rim of the wedge (due to imperfections in the manufacturing process (12)) and the force-induced deflection of the cantilever. We estimate a total error of cell height of $\approx$0.5 μm due to unevenness of the cantilever wedge and vertical movement of the cantilever to a position above the cell. The analysis of experimentally measured ΔF in dependence of ξ is described in detail in Section S2 in the Supporting Material.

Oscillatory compression of cells

To sample the viscoelastic response of cells at a distinct frequency, we performed oscillatory compressions of cells. To this end, we sandwiched cells between dish bottom and cantilever wedge and carried out oscillatory height modulations of the AFM cantilever with typical oscillation amplitudes of 0.1–0.5 μm in a frequency range of 0.01 and 2 Hz (Supporting Material). During this procedure, the cell was on average kept at a normalized height reduction of 30–40%. Oscillatory cantilever height modulations were generated by a piecewise linear approximation of the sine-function for oscillation periods of 0.5, 1, 5, 10, 50, and 100 s in a piezo height control mode (Supporting Material). If not indicated otherwise, height oscillations were set to an amplitude of 0.5 μm. If force oscillations became large (force minima reaching <50% of the average force value), oscillations were repeated at 0.25-μm amplitude. In this case, the lower-amplitude oscillations were used for stiffness analysis. We also performed cantilever oscillations in the absence of a cell. These blank cantilever oscillations also generated force oscillations. In this case, however, force amplitudes were much smaller ($\lesssim$0.02 nN). Accordingly, effects of the medium's viscosity are negligible. Oscillatory force and cantilever height curves were analyzed in the following way: for every data point, effective tension γ_{eff} and surface area strain $(A(t) - \langle A\rangle)/\langle A\rangle$ are estimated. An amplitude and a phase angle associated to the oscillatory time variation of effective tension γ_{eff} and surface area strain are extracted (Supporting Material). To estimate the value of the complex elastic modulus at a distinct frequency, we determine the phase angles φ_γ and φ_{ϵ_A} as well as amplitudes $\widehat{\gamma}_{\mathrm{eff}}$ and $\widehat{\epsilon}_A$ of effective tension and surface area strain, respectively. The complex elastic modulus at this frequency is then calculated as $\widehat{\gamma}/\widehat{\epsilon}_A \exp^{i(\varphi_\gamma - \varphi_{\epsilon_A})}$. In cells treated with a combination of latrunculin A (200 nM) and blebbistatin (10 μM), surface tensions were very low and mitotic cells were not properly rounded if adhered to the cell culture dish. Therefore, rheological measurements were performed on PEG-coated dishes in this condition (Table 1, row 6). Cantilever oscillations were chosen as 0.5 μm by default to achieve an acceptable signal/noise.

Restoration of myosin activity through photoinactivation of blebbistatin

Rheological measurements including (indirect) photoactivation of myosin II in blebbistatin-treated cells were performed on PEG-coated dishes with detached cells. In this way, we could entirely rule out effects of cell shape changes and adhesion during changing cell surface tension. During photoactivation measurements, we performed cantilever height oscillations until force oscillations were in steady state. Then, we exposed the cell for $\approx$10 s to blue light (GFP excitation, fluorescence lamp). As a consequence, the measured AFM force shoots up and at the same time, oscillation amplitudes increase (see Fig. 6 *a*). Then, over a time interval of $\approx$10 min, the average force gradually decreases back to its original value as active blebbistatin reenters the cell (see Fig. 6 *a*). As this decrease is slow as compared to the sampled oscillation periods (1, 10 s), we expect that oscillations are close to steady state during this time interval. We determined the momentary complex elastic modulus and the average effective tension within moving time windows of two oscillation periods. Oscillation amplitudes were chosen to be very

Please cite this article in press as: Fischer-Friedrich et al., Rheology of the Active Cell Cortex in Mitosis, Biophysical Journal (2016), http://dx.doi.org/10.1016/j.bpj.2016.06.008

TABLE 1 Rheological Parameters of Cells In Different Measurement Conditions

	τ_{max} (s)	*p*-value (for τ_{max})	K_h (mN/m)	*p*-value (for K_h)	γ_{st}(mN/m)	*p*-value (for γ_{st})	ξ	*N*
Control	13.8 ± 5.2	1	18 ± 4.6	1	1.67	1	0.36	9
Blebbistatin 2.5 μM	24.3 ± 5.8	0.002	10.3 ± 2.7	0.0004	0.54	3e-4	0.38	9
Y-27632 5 μM	31 ± 10.5	0.004	6.6 ± 2.1	0.001	0.45	0.002	0.36	6
Control	12.9 ± 4.1	1	19.8 ± 8.2	1	1.9	1	0.36	19
Taxol 100 nM	8.5 ± 3	0.001	23.4 ± 11.6	0.3	2.2	0.04	0.37	20
Control	11.7 ± 4.3	1	24.4 ± 9.4	1	1.88	1	0.33	9
Nocodazol 100 nM	10 ± 2.8	0.33	27.3 ± 7.55	0.37	2.3	0.02	0.36	9
Control, *F-Luc* (RNA_i)	7.66 ± 3.2	1	25.7 ± 8.6	1	1.98	1	0.4	9
MYH9 (RNA_i)	21.8 ± 10.6	0.006	10.9 ± 2.4	0.0015	0.68	3e-4	0.39	9
Control, *F-Luc* (RNA_i)	8.3 ± 1.8	1	26.5 ± 5.4	1	2.2	1	0.35	10
ACTN4 (RNA_i)	4.7 ± 2.33	0.002	22.7 ± 6.5	0.11	1.7	0.02	0.36	12
Control	13.2 ± 3.5	1	20.9 ± 6.3	1	2.1	1	0.34	12
Latrunculin A 200 nM + blebbistatin 10 μM	4 ± 1.9	1e-5	1.3 ± 0.6	4e-5	0.06	1e-23	0.39	14

Parameter values K_h and τ_{max} were fit for each cell measured individually. Shown are average values and SDs. *P*-values were calculated using a Mann-Whitney test. In addition, mean values of cell surface tension γ_{st} and cell height reduction ξ are indicated. During measurements, cells were adhered to glass-bottom dishes except for measurements corresponding to row 7. There, cells were detached before the measurement and resuspended on PEG-coated dishes to ensure proper cell rounding at very low surface tension (Materials and Methods). Blebbistatin inhibits myosin II; Y-27632 inhibits ROCK, which then affects cortical myosin activity downstream; taxol stabilizes microtubules; nocodazol interferes with microtubule polymerization; and latrunculin A interferes with actin polymerization. Lat. A, latrunculin A; blebb., blebbistatin.

small (0.125 μm) such that the average effective tension could to a good extent be identified with cell surface tension at steady state.

Gene knock-down through RNA interference

To probe the influence of the molecular composition of the cell cortex on the viscoelastic response of cells, we performed gene knock-downs through RNA interference. Cells were transfected with esiRNA (eupheria) targeting the genes *MYH9* and *ACTN4* at a concentration of 10 nM (*MYH9*) and 100 nM (*ACTN4*), respectively, using the transfection reagent Lipofectamin RNA_iMAX (Invitrogen). For a control, we used firefly luciferase esiRNA (*F-Luc*). At day 0, 30,000 cells were seeded into a 24-well plate (Nunc MicroWell Plates with Nunclon; Thermo Fisher Scientific, Waltham, MA). Transfection was carried out at day 1, medium was exchanged at day 2 (without antibiotics), and transfected cells were measured at day 3. Approximately 12 h before measurements, cells were trypsinized, diluted, and transferred onto a glass-bottom petri dish (FD35; World Precision Instruments) to achieve a confluency of 20–40% during AFM measurements.

Estimating cellular shape and volume during AFM measurements

During progressive uniaxial cell compression, a time-lapse of z-stacks was recorded in DIC mode including eight z planes centered roughly around the cell equator ($\Delta t = 10$–20 s and $\Delta z = 1$ μm). At each compression level, we chose a time point of the time series, where steady force was reached and selected the z plane with maximal cell diameter and used this as an estimate of equatorial cell radius. It has been shown previously that the shape of mitotic cells during parallel plate confinement is to a very good approximation given by a shape of minimal surface area at negligible adhesion (10). Therefore, the equatorial cell radius R_{eq} and cell height h are sufficient parameters to determine cell shape and cell volume (Fig. S9) (10,16). To calculate cell volume, we used the formula $V = -(\pi/24)h(h^2(3\pi - 10) - 6h(\pi - 4)R_{eq} - 24R_{eq}^2)$, which can be derived by approximating the profile of the free cell contour by a semicircle. In this way, we estimated cell volume for progressive cell compression levels. In general, we do not find a trend for increasing or decreasing cell volume due to progressive uniaxial cell compression within the uncertainties of our measurement ($\approx$2% error; see Fig. S10). Therefore, we averaged volume values of one cell measured at the first four compression levels and used this average volume as estimated cell volume. Cells that were sampled through oscillatory uniaxial compression were imaged during slow cantilever oscillations ($f = 0.01$ or 0.02 Hz) and the average equatorial radius during oscillations was determined. The average radius together with average cantilever height during oscillations was used to estimate cell volume as described above. Anticipating shapes of minimal cell surface area in steady state of uniaxial cell compression, we could calculate the area of contact $A_{con} = \pi r_{con}^2$ between cell and cantilever wedge (or dish bottom) and the mean curvature H of the free cell surface for each compression level (Fig. S9). To determine the contact radius r_{con}, we used the approximative formula $r_{con} = (R_{eq} - (h/2)) + (2/3)(\sqrt{(2R_{eq}^3 - hR_{eq}^2)}/\sqrt{(h + 2R_{eq})} - (R_{eq} - (h/2)))$, described in Fischer-Friedrich et al. (10). Together with measured AFM forces, this allowed us to estimate cell surface tension in steady state (10).

Calculations of the uniaxial compression of elastic model cells

To distinguish between the scenario of a mechanically dominant cell interior or cell cortex, we performed calculations of elastic deformations in idealized model cells. We calculated the elastic deformation of model cells in two different scenarios with the aid of Comsol Multiphysics (https://www.comsol.com/; see the Supporting Material for details). In the first scenario, which represents a mechanically dominant cytoplasm, the model cell was represented by an elastic body of revolution ($E = 1000$ Pa, $\nu = 0.49$) generated by a rectangle and an adjacent semicircle (see *black wire-frame* in Fig. 2 *a*). In the second scenario, which represents a mechanically dominant cortical layer, the model cell was represented by an elastic shell ($E = 125$ kPa, $\nu = 0.49$) whose shape was defined by an outer contour of minimal surface area and a thickness of 200 nm (10). Furthermore, we assigned a uniform, constant mechanical prestress that mimics active tension in the cortex due to the presence of myosin motors. The prestress is a constant, isotropic in-plane stress in the shell that was set to 5000 Pa corresponding to a surface tension of $\gamma_{st} = 1$ mN/m. We calculated the force increase ΔF due to the creation of elastic stresses after a uniaxial compression by Δh resulting from a set piezo displacement of 0.5 μm. The total cell volume for both scenarios was $V = 5000$ μm and was kept constant during the

Please cite this article in press as: Fischer-Friedrich et al., Rheology of the Active Cell Cortex in Mitosis, Biophysical Journal (2016), http://dx.doi.org/10.1016/j.bpj.2016.06.008

deformation. In the case of a shell, volume conservation was realized by the implementation of an internal pressure that was adjusted in the process of compression. In our calculations, objects are initially free of elastic stresses and only after the performance of the compression step are elastic stresses present. Calculations were carried out with elastic reference shapes with varying cell height h corresponding to different values of cell height reduction $\xi = 1 - h/(2R)$, where $R = (3/(4\pi)V)^{1/3}$. We find that the functional dependence of $\log(\Delta F/\Delta h)(\xi)$ is close to linear (see Fig. 3 *a*). Linear slopes fitted in the ξ-interval [0.2, 0.6] differ for the two scenarios: while the elastic bulk shows a slope of $\approx$5.5, the elastic shell displays a slope of $\approx$9.7 (see Fig. 3 *a*). Simply speaking, the larger slope of $\log(\Delta F/\Delta h)(\xi)$ for the case of the shell originates from surface area stretch ($\Delta A/A$) increasing more strongly than bulk strain ($\approx \Delta h/h$) for increasingly oblate equilibrium shapes. These distinct trends allow us to clearly discriminate between the two scenarios of a bulk- or a shell-dominated mechanics. To compare theoretical results with experimental data, we plotted $\log(\Delta F/\Delta h)(\xi)$ for each cell measured and fit a linear slope (see Fig. 3 *b*). Indeed, measured $\log(\Delta F/\Delta h)(\xi)$ are captured well by a linear dependence and show average slopes of 10.1 $\pm$ 1.2 for untreated, mitotic cells (see Fig. 3, *b* and *c*, *green*, 0.5 μm piezo displacement, Δt = 1 s, N = 11). We also measured cells treated with low doses of blebbistatin (2.5 μM), which leads to a reduction of cell surface tension by inhibition of myosin II. Again, we performed iterative cell compression steps on those cells. There, $\log(\Delta F/\Delta h)(\xi)$ follows on average a slope of 10.1 $\pm$ 0.8 (see Fig. 3, *b* and *c*, *red*, N = 11). Comparing slopes as predicted from computer simulations (slope of $\approx$5.5 for elastic bulk and slope of $\approx$9.7 for elastic shell) with experimentally derived slopes, we concluded that the experimental data are significantly closer to the scenario of a compressed shell (see Fig. 3 *c*).

RESULTS

Rheology of thin active films

We first discuss the mechanics of a thin active film as a model for the cell cortex. The cortex is a dynamic active gel. While myosin and cortical cross-linker proteins turn over on timescales on the order of 1–10 s, actin filaments in the mitotic cortex turn over on the timescale of roughly 1 min (2,17). In the steady state, actomyosin contractility generates an in-plane contractile tension, the cortical tension denoted γ_{st}. Under dynamic area changes, this film tension becomes a dynamic quantity. The rheology of the film under uniform area dilation is characterized to linear order as

$$\gamma_{tot}(t) = \int_{-\infty}^{t} G_{2D}(t-t')\dot{\epsilon}_A(t')dt' + \gamma_{st}, \qquad (1)$$

where $\epsilon_A(t) = (A(t) - A_0)/A_0$ is the area strain, A_0 is a reference area, and the dot denotes a time derivative. The relaxation modulus $G_{2D}(t)$ describes the time-dependent response, including memory effects and viscoelastic material properties (18). Equation 1 describes a relaxation process by which the film tension relaxes to the steady-state value γ_{st}. The relaxation modulus $G(t)$ results in general from a superposition of many collective relaxation modes with a range of relaxation times τ, and can thus be written as (18)

$$G_{2D}(t) = \int_{-\infty}^{\infty} h(\tau)\exp(-t/\tau)d\ln(\tau). \qquad (2)$$

Here, the relaxation spectrum $h(\tau)$ characterizes the relative weight of modes with relaxation time τ. The function $h(\tau)$ characterizes the mechanical properties of the material. In the absence of detailed knowledge of the internal relaxation processes, we use a simple choice of $h(\tau)$, which corresponds to a relaxation spectrum with constant amplitude up to a maximal time τ_{max}, which is the longest relaxation time (Fig. S1 *a*). In short, we choose $h(\tau) = K_h$ for $\tau \leq \tau_{max}$ and $h(\tau) = 0$ for $\tau > \tau_{max}$. With this choice, the relaxation modulus is given by the Supporting Material as

$$G_{2D}(t) = -K_h Ei(-t/\tau_{max}), \qquad (3)$$

where $Ei(z) = -\int_{-z}^{\infty} \exp(-t)/t dt$ is called the exponential integral. The complex elastic modulus $G^*_{2D}(\omega) = \int_0^{\infty} G_{2D}(t) i\omega\, e^{-i\omega t} dt$ can be decomposed into a real and an imaginary part as $G^*_{2D} = G'_{2D} + iG''_{2D}$ with

$$G'_{2D}(\omega) = \frac{K_h}{2}\log\left(1 + (\tau_{max}\omega)^2\right), \qquad (4)$$

$$G''_{2D}(\omega) = K_h \arctan(\tau_{max}\omega). \qquad (5)$$

This complex elastic modulus characterizes the frequency-dependent response of the active film to area dilation. The real-part G'_{2D} is a two-dimensional (2D) storage modulus that accounts for the in-phase elastic response. The imaginary part G''_{2D} is a 2D loss modulus that accounts for a viscous response. This dissipative part of the response is phase shifted to the applied oscillatory stress by $\pi/2$. Alternatively, the complex modulus can also be written as $G^*_{2D} = |G^*_{2D}|\exp(i\varphi)$, where the phase φ describes the lag between stress and strain during oscillatory forcing of the material. For viscoelastic materials, this phase shift typically ranges between zero and $\pi/2$. If the material is solid-like, the phase shift is small and close to zero. Viscous behavior corresponds to a phase shift close to $\pi/2$. Equations 4 and 5 provide a simple model to discuss the rheology of the cortical layer based on a characteristic timescale and a complex elastic modulus.

Note that the general form of the relaxation modulus given by Eq. 3 is model-independent. A particular choice of the relaxation spectrum $h(\tau)$ corresponds to a rheological model. For example, the Maxwell model corresponds to the choice $h(\tau) = K\delta(\tau - \tau_0)$, where τ_0 is the Maxwell time and K is an elastic modulus. Our choice of the relaxation spectrum giving rise to the moduli (3–5) captures the essential features of the experimental data using only two parameters. Note that our model is fundamentally different from the Maxwell model as it captures a broad spectrum of relaxation processes. Power laws are often used to fit experimental data. Power laws also imply the existence of a broad relaxation spectrum. However, in the presence of a maximal relaxation time of the system, the power law must be cut off (Section S1). In the cortex, a maximal

Please cite this article in press as: Fischer-Friedrich et al., Rheology of the Active Cell Cortex in Mitosis, Biophysical Journal (2016), http://dx.doi.org/10.1016/j.bpj.2016.06.008

relaxation time exists because of filament turnover. As discussed in Results, a power-law relaxation spectrum without cutoff does not provide a good fit to the data.

Cell compression between two parallel plates

To experimentally characterize the mechanics of the cell cortex, we probed the mechanical response of HeLa cells in mitotic arrest utilizing AFM together with wide-field imaging. Cells were chemically arrested in mitosis by addition of STC, an inhibitor of kinesin Eg5. In this way, arrested cells were adopting a rounded shape for several hours. During our measurements, these rounded cells were confined between the cell culture dish and an AFM cantilever that was supplemented with a wedge (10,12) (Fig. 1 *a*). To characterize the confined cell shape during our measurements, we introduce the variable normalized cell height reduction $\xi = 1-h/(2R)$, which quantifies how much the perturbed cell height h deviates from that of a sphere of equal volume $(R = (3/(4\pi)V)^{1/3}$, where V is the measured cell volume; see Materials and Methods). This variable takes the value 0 if the cell shape is spherical and 1 if the cell is squeezed entirely to the dish bottom. After confining a cell with the cantilever, we waited until a steady state was reached with a constant force F_{st} exerted on the cantilever. This steady-state force F_{st} can be attributed to the presence of a cell surface tension $\gamma_{st} = F_{st}/(2H\pi r_{con}^2)$, where r_{con} is the radius of the cell contact area on the plates and H is the mean curvature of the cell surface (10,16). While γ_{st} is largely constant independent of the confinement height of the cell, the steady state force F_{st} increases for increasing ξ (10). We estimated the cell volume at increasing levels of cell height reduction and did not observe volume changes (within the accuracy of our measurements), suggesting that the cell volume is constant during the experiments (Fig. S10).

Using the AFM-based assay, we performed step strain experiments by uniaxially compressing the cell in a series of small steps Δh (Fig. 1, *a* and *b*). Upon each compression step, we observed a rise in force F up to a peak value F_{max}. After the step was completed, the force relaxed to a new steady-state value F_{st} that corresponds to the new cell height (Fig. 1 *b*). We thus denote the force difference $\Delta F = F_{max} - F_{st}$ as transient force increase (Fig. 1 *b*). An example of the force relaxation upon a compression step is shown in Fig. 1 *c* (*solid lines*), together with a fit of the model given by Eq. 3 (for details, see the Supporting Material). The inset shows a semilogarithmic plot of the same data. The observed force relaxation is similar to previous reports (11) and indicates a viscoelastic response of the cell. From the fact that tension relaxes to a value set by the steady cortical tension, we conclude that elastic stresses relax completely after a finite relaxation time.

Viscoelastic cell stiffness is dominated by the cortical layer

The AFM measurements show that we can characterize the time-dependent mechanical properties of the cell. We next wanted to understand the contribution of the cortical layer to these mechanical properties. For this purpose, we performed calculations of the uniaxial compression of two types of elastic model cells. The first model cell was constituted by an incompressible shear-elastic bulk (Fig. 2 *a*). This corresponds to the extreme case of a cell with an elastic cytoplasm that dominates the mechanical properties. The second model cell was constituted by an elastic shell enclosing an incompressible bulk (Fig. 2 *b*). This corresponds to the extreme case of an elastic cortical layer that dominates cell mechanics. This elastic picture, although simplified compared to the cell, allows us to characterize the differences of cortical and cytoplasmic contributions to cell mechanics.

Calculations were performed using linear elasticity theory in terms of finite element simulations (Materials and Methods and see the Supporting Material). For both cell models, we started from a stress-free reference shape with reduced height $h = 2R(1-\xi)$. We deformed each model cell through a step of uniaxial compression by $\Delta h = 0.5$ μm

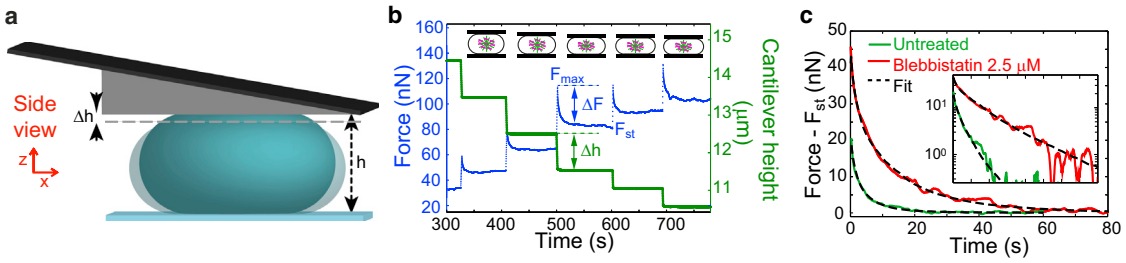

FIGURE 1 Stepwise uniaxial compression of a mitotic cell. (*a*) Schematic of a compressed cell (*blue*) confined between the dish bottom and a wedged AFM cantilever. In a compression step, the cantilever is lowered by a height interval Δh. (*b*) Measured compression force and cantilever height during stepwise uniaxial cell compression. (*c*) Force relaxation after a step of uniaxial cell compression (normalized cell confinement) for an untreated cell (*green*) and a cell treated with the myosin II inhibiting drug blebbistatin (2.5 μM, *red*). The steady-state value has been subtracted. (*Dashed lines*) Fit of the rheological model (untreated: $\xi = 0.47$, $\tau_{max} = 11.5$ s, $K_h = 12.7$ mN/m, and $F_{st} = 130$ nN; blebbistatin-treated: $\xi = 0.55$, $\tau_{max} = 35$ s, $K_h = 10.3$ mN/m, and $F_{st} = 40$ nN). (*Inset*) Same data as in (*c*) in a semi-log plot. Before measurements, cells were arrested in mitosis by addition of S-trityl-L-cysteine (2 μM). To see this figure in color, go online.

BPJ 7419

Please cite this article in press as: Fischer-Friedrich et al., Rheology of the Active Cell Cortex in Mitosis, Biophysical Journal (2016), http://dx.doi.org/10.1016/j.bpj.2016.06.008

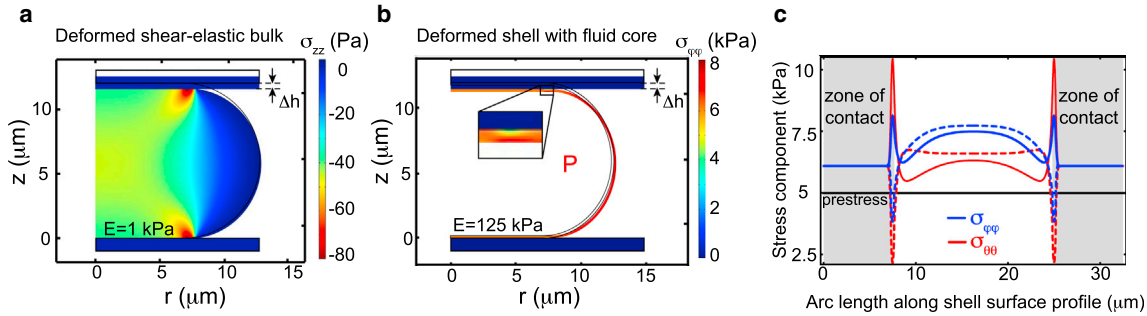

FIGURE 2 Finite element simulations of uniaxial compression of elastic model cells (*side view*, $\Delta h = 0.5$ μm). (*a*) First model cell consisting of a uniform, shear-elastic bulk ($E = 1$ kPa) with undeformed shape given by a body of revolution generated by a semicircle displaced orthogonally from the axis of revolution (*black wire-frame*, volume: 5000 μm^3). The deformed configuration is shown as a colored area. Color-codes for the magnitude-of-stress component σ_{zz}. (*b*) Second model cell constituted by a shear-elastic shell enclosing a constant volume ($E = 125$ kPa, Poisson ratio $\nu = 0.49$, thickness 200 nm) and with a constant in-plane prestress (5 kPa) corresponding to a constant active tension of ≈ 1 mN/m. This active tension is balanced by an internal pressure P. The shape before deformation is indicated by a black wire-frame and corresponds to a shape of minimal surface area at a given volume of 5000 μm^3. The colored area shows the deformed shell. Color-codes for the value of stress component $\sigma_{\varphi\varphi}$, where φ is the azimuthal angle. As the problem is axisymmetric, only one-half of the cell is shown corresponding to azimuthal angle $\varphi = 0$. (*c*) Stress components $\sigma_{\varphi\varphi}$, and $\sigma_{\theta\theta}$, in the compressed shell along the contour of the inner (*solid*) and outer (*dashed*) surface of the shell (starting from the center of the contact area and continuing up to the equator). While φ denotes the azimuthal angle, θ parameterizes the direction orthogonal to φ in the tangent plane of the shell surface. Shown is the overall stress (prestress + elastic stress). To see this figure in color, go online.

and calculated the transient force increase ΔF due to elastic stresses. The two scenarios show different behaviors of ΔF as a function of the normalized cell height reduction ξ (Fig. 3 *a*). Therefore, the simple alternatives of bulk- or shell-dominated mechanics can be clearly discriminated from the slope of $\log(\Delta F/\Delta h)$ upon compression.

In contrast to the ideal elastic model cell, actual cells are viscoelastic and their effective stiffness is timescale-dependent. However, for step strain experiments, a direct analogy can be drawn between an elastic and a viscoelastic system if the strain is applied in a fixed time interval and therefore a particular range of timescales of the system is probed (Section S3). We therefore examined whether experimentally measured ΔF, which is the transient force increase due to the presence of elastic stresses, shows a dependence on normalized cell height reduction that corresponds to either of the two elastic model cells. We plotted $\Delta F/\Delta h$ versus ξ in a semilogarithmic plot comparing the obtained slopes to those obtained from computer simulations (Fig. 3 *b*). Using histograms of the experimental slopes, we conclude that the experimental data are close to the scenario of a compressed shell (Fig. 3 *c* and Materials and Methods). This suggests that the cortical layer is the dominant mechanical element in the mitotic cell. Thus, the mechanical cell

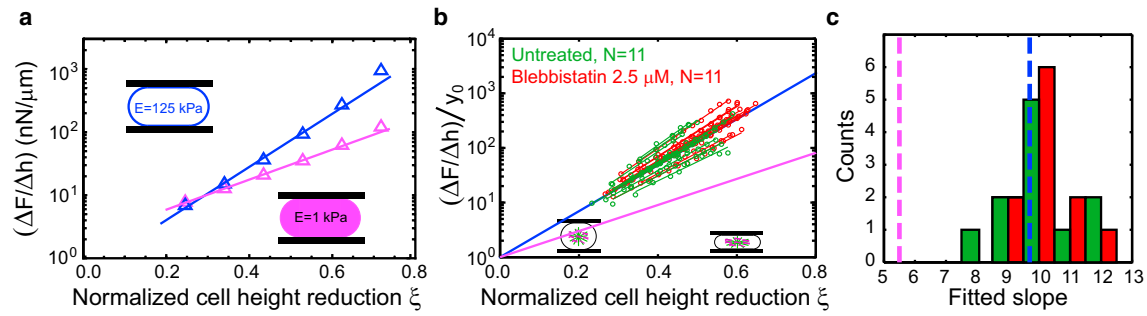

FIGURE 3 Behavior of the cellular force response to compression steps for different cell compression levels in model cells and experiments. (*a*) Calculated, normalized force increase ΔF due to elastic stresses in model cells of different initial reference shapes as a function of normalized cell height reduction $\xi = 1 - h/(2R)$, where h is the initial cell height and $R = (3/(4\pi)V)^{1/3}$ for cell volume V (Fig. 2, shear-elastic bulk: *magenta*, elastic shell: *blue*, $\Delta h = 0.5$ μm). Every data point was calculated for an elastic object with $V = 5000$ μm^3, which corresponds to a typical volume of a mitotic HeLa cell. (*b*) Comparison of normalized force increase from measurements and theory. Every cell was measured at different cell heights giving rise to 5–10 measured values $\Delta F(\xi)$ per cell (*circles*). Experimental data points from one cell are fit linearly (untreated cells: *green*, $N = 11$; cells treated with 2.5 μM blebbistatin, *red*, $N = 11$, 0.5 μm piezo displacement). The lines in blue and magenta represent the linear fit presented in (*a*). All curves were normalized by division through their y intercept y_θ as estimated from a linear fit. (*c*) Histogram of fit slopes of the measured curves $\log(\Delta F(\zeta)/\Delta h)(\xi)$ for untreated cells (*green*) and blebbistatin-treated cells (*red*). Dashed lines indicate the slopes as predicted by FEM simulations for the scenario of an elastic shell with active tension (*blue line*) or the scenario of an elastic bulk (*magenta*). All measured cells were mitotically arrested by addition of STC (2 μM). To see this figure in color, go online.

Please cite this article in press as: Fischer-Friedrich et al., Rheology of the Active Cell Cortex in Mitosis, Biophysical Journal (2016), http://dx.doi.org/10.1016/j.bpj.2016.06.008

response shown in Fig. 1 provides information about the rheology of the cell cortex.

Oscillatory forcing of the cell cortex

We next performed a careful rheological analysis of the cortical layer in mitosis using cell compression. A cortical layer is a complex and interlocking set of mechanical elements that responds under uniaxial compression at different timescales. To distinguish the mechanical behavior at different timescales, we performed experiments in which the cell height was oscillated at different frequencies (Fig. 4 *a*). These height modulations give rise to an oscillatory force response of the cell with a phase difference between the cantilever height oscillation and the cellular force response. We observed that force oscillation amplitudes increase for higher frequencies at constant height amplitude (Fig. 4 *b*). This implies that cell stiffness is larger at shorter timescales consistent with the observed larger forces at shorter times in Fig. 1 *b*. Force oscillations were close to a sinusoidal shape and scaled linearly with the amplitude of cantilever height oscillations (Fig. 4, *a* and *c*; Fig. S12). Therefore, we conclude this to be in the regime of linear viscoelastic behavior. Note that when the cortex was disintegrated by cytoskeletal drugs, we observed strongly reduced force oscillation amplitudes (Fig. 4 *b*, *red data*), consistent with the finding that the cortex dominates cell mechanics.

For a rheological analysis, we identified strain and stress variables in our experiments. The results of the previous section indicated that the cellular viscoelastic response is dominated by the cortical layer. We therefore chose the strain variable to be the area strain of the total cell surface area (see Section S4). The relevant stress is the instantaneous cortical tension. To estimate this tension, we used an effective tension γ_{eff} given by the normalized AFM force $F(t)/(2H(t)\pi r_{\mathrm{con}}^2(t))$. In steady state, the effective tension equals the cell surface tension γ_{st}. Force amplitudes approach a nonvanishing value for small frequencies. However, amplitudes of effective tension γ_{eff} approach zero in this limit (Fig. 4 *b*, *lower panel*).

Defining stress and strain as described above, we could deduce a complex elastic modulus of the 2D cell cortex. Measured cortex elastic moduli for untreated cells are shown in Fig. 5 together with a fit of the model defined in Eqs. 4 and 5. For untreated cells in mitotic arrest, we obtained from this fit the parameters $\tau_{\max} = 14 \pm 6$ s and $K_h = 18 \pm 8$ mN/m ($N = 95$), where errors indicate SDs. In the log-log plots shown in Fig. 5, *b* and *c*, fits of a Maxwell model and of a power law to the experimental data are also shown. As expected, the Maxwell model does not correctly account for the data. Furthermore, our rheological model provides a better fit of the data than a power law.

We tested whether measured values of the complex modulus $G^*_{2\mathrm{D}}(\omega)$ depend on the degree of normalized cell height reduction ξ. We found that the magnitude of $G^*_{2\mathrm{D}}(\omega)$ decreases for increasing ξ (Fig. S5 and Section S7). Therefore, to investigate the effect of perturbations on the stiffness of cells, it is important to perform measurements at similar normalized cell height reduction ξ.

When oscillatory cell forcing was applied in the same way to rounded interphase cells, we obtained qualitatively similar rheological data which were still captured by our model (Fig. S17). However, cortex stiffness values as reflected by K_h were roughly one order of magnitude smaller ($K_h = 1$ mN/m and $\tau_{\max} = 8$ s). A similar relative increase in stiffness from interphase to mitosis was reported earlier from AFM indentation experiments on *Drosophila* S2R$^+$ cells (19).

So far, we have presented 2D complex elastic moduli of the cell cortex in units of mN/m for mitotic cells. To compare our results with previous measurements that showed three-dimensional (3D) complex elastic moduli of

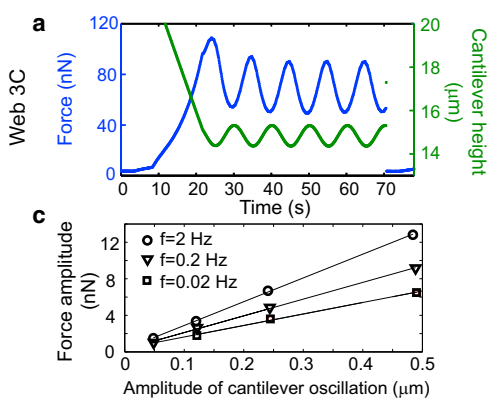

FIGURE 4 Rheological characterization of the mitotic cortex through oscillatory cell compression. (*a*) Exemplary readout of cantilever height and AFM force during rheological cell probing. The AFM cantilever is lowered onto the cell and sinusoidal cell height oscillations are imposed (*green curve*). Steady force oscillations emerge after a transient phase (*blue curve*). (*b*, *Top*) Force oscillation amplitudes (*blue curve*) depend on frequency. For slow oscillation frequencies, force amplitudes approach the value expected from purely geometrical changes (*dashed line*) at constant cell surface tension. Exposing cells to a combination of the actin-depolymerizing drug latrunculin A (200 nM) and the myosin II-inhibiting drug blebbistatin (2.5 μM), force oscillation amplitudes (*red curve*) are strongly reduced. (*b*, *Bottom*) Associated oscillation amplitudes of effective tension $\gamma_{\mathrm{eff}} = F/(A_{\mathrm{con}}2H)$. Cantilever oscillations amplitudes were set to 0.5 μm. Error bars indicate SDs. (*c*) Force amplitudes increase linearly with cantilever oscillation amplitudes in the measured frequency range. To see this figure in color, go online.

Please cite this article in press as: Fischer-Friedrich et al., Rheology of the Active Cell Cortex in Mitosis, Biophysical Journal (2016), http://dx.doi.org/10.1016/j.bpj.2016.06.008

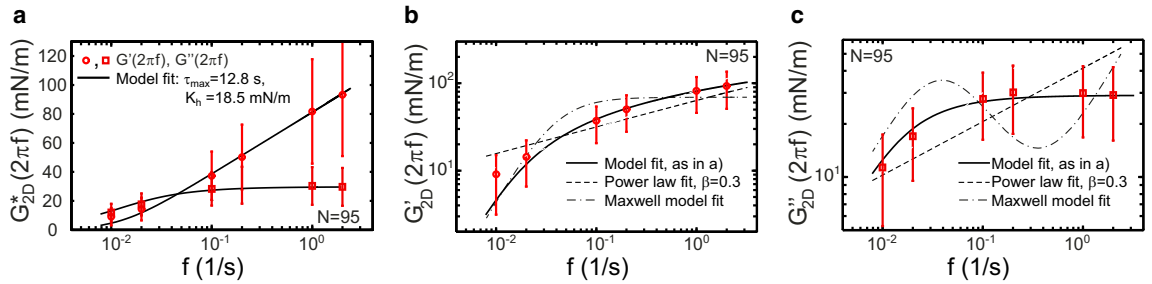

FIGURE 5 Two-dimensional, complex elastic modulus obtained from rheological sampling of mitotic cells. (*a*) Averaged storage (*circles*) and loss modulus (*squares*) in dependence upon frequency ($N = 95$ cells). To calculate elastic moduli, effective tension ($\gamma_{\mathrm{eff}} = F/(A_{\mathrm{con}}2H)$) was identified with stress, while estimated area strain of overall cell surface area was identified with strain. Storage and loss modulus were fit simultaneously assuming a constant relaxation spectrum $h(\tau)$ of constant magnitude K_h up to a cutoff time $\tau_{\max}$. Obtained fit parameters were $K_h = 18.5$ mN/m and $\tau_{\max} = 12.8$ s (*solid black lines*). (*b* and *c*) Averaged storage and loss modulus in a log-log representation (same data as in *a*) and associated model fits: our model (*solid black line* as in *a*); power law (*dashed line*); and Maxwell model with viscous element (*dash-dotted line*). For the power-law fit, fit functions were $G'_{2\mathrm{D}}(\omega) = A\omega^{\beta}, G''_{2\mathrm{D}}(\omega) = B\omega^{\beta}$ with fitted parameter values $A = 36.4$ mN/m•s$^{\beta}$, $B = 23.6$ mN/m•s$^{\beta}$, and $\beta = 0.3$. For the Maxwell-model fit, fit functions were $G'_{2\mathrm{D}}(\omega) = k\omega^2\tau^2/(1+\omega^2\tau^2)$ and $G''_{2\mathrm{D}}(\omega) = k\omega\tau/(1+\omega^2\tau^2) + \eta$ with fitted parameters $k = 69.22$ mN/m, $\tau = 4.16$ s, and $\eta = 3.25$ mN s/m. Error bars indicate SDs. To see this figure in color, go online.

cells, we also performed an alternative analysis of our data calculating effective 3D Young's moduli using normalized cell height as strain and defining stress as $\sigma = F/A$, where F is the force and A is the cell cross-sectional area (Fig. S8, *a* and *b*). From this analysis, we obtain effective frequency-dependent cell elastic moduli in the range of 100–1500 Pa for mitotic cells. For interphase cells, we obtain values in the range 10–500 Pa that are comparable to effective cell elastic moduli reported earlier for rounded interphase cells (20,21). Note, however, that effective 3D cell elastic moduli are not appropriate to describe 2D cortical mechanics. Interestingly, these effective 3D cell elastic moduli as a function of frequency resemble a power law more closely than the 2D moduli describing cortical rheology (compare Fig. S8, *a* and *b* to Fig. 5, *b* and *c*). The reason for the altered shape of the dynamic moduli as a function of frequency originates in the different choice of the stress variables in the definitions of elastic moduli. In the case of effective 3D moduli, the stress variable is the scaled force, while in the case of 2D moduli, it is the cortical tension. Time-dependent force and cortical tension are not just proportional to each other. They are phase-shifted because of the coupling of the time-dependent cell geometrical changes with the active cortical tension in the force balance (see Section S9 for details). Therefore, elastic moduli derived from force or tension oscillations, respectively, show a different frequency-dependence.

Modulation of rheological properties by molecular perturbations

Having set up this method to study time-dependent cortex rheology during mitosis, we wanted to examine the influence of different molecular perturbations in the cellular system. To this end, we used cytoskeletal drugs and gene knock-down by RNA interference. For each condition, we determined the parameters $\tau_{\max}$ and K_h by fitting the rheological model to the frequency-dependent storage and loss moduli for each cell.

We found that perturbations of the cortex-associated molecular motor myosin II had a clear influence on cortex rheology. After addition of the myosin II perturbing drugs blebbistatin (selective inhibitor of non-muscle myosin II) and Y-27632 (selective inhibitor of ROCK, which regulates myosin II activity (11,22)), and after knock-down of myosin II, storage and loss moduli decreased (Fig. S13). The associated phase shifts also decreased. Correspondingly, the cutoff time $\tau_{\max}$ increased and the spectrum amplitude K_h decreased (Table 1, rows 1 and 4; Fig. S13). These results indicate that reduction of myosin II activity makes the cell cortex more solidlike but less stiff.

To further examine the effect of myosin activity on cortical rheology, we used photoinactivation of the myosin II inhibitor blebbistatin under conditions were myosin was initially inhibited by blebbistatin (2.5–5 μM). Because blebbistatin is photo-inactivatable by blue light (23), myosin II activity could be restored by blue light exposure. During oscillatory cell compression, the average force increased rapidly upon illumination by blue light (Fig. 6 *a*). The amplitude of force oscillations also increased. When illumination was switched off after ~10 s, the average force gradually relaxed to its original value after ~10 min as active blebbistatin reentered the cell (Fig. 6 *a*). In this time interval, we determined rheological properties of a cell while cell surface tension changed gradually because of myosin reinhibition (Materials and Methods). We found that the magnitude of the complex elastic modulus $\left|G^*_{2D}(\omega)\right|$ and the phase shift φ between stress and strain decreased roughly linear together with the declining cell surface tension (Fig. 6 *b*; Fig. S15). This indicates a more fluidlike behavior for higher values of active tension. Using values of $G^*_{2\mathrm{D}}(2\pi f)$ measured at $f = 0.1$ and 1 Hz, we estimated

Please cite this article in press as: Fischer-Friedrich et al., Rheology of the Active Cell Cortex in Mitosis, Biophysical Journal (2016), http://dx.doi.org/10.1016/j.bpj.2016.06.008

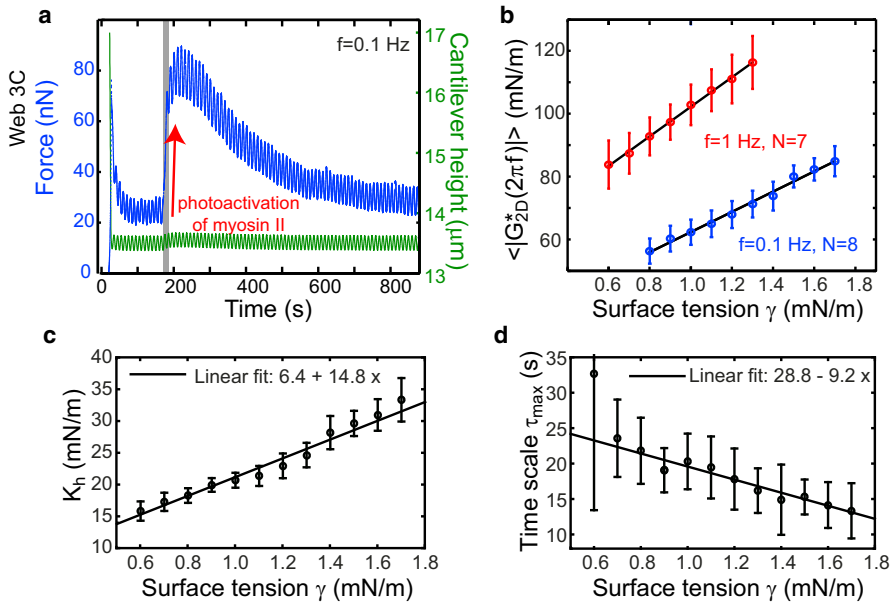

FIGURE 6 Mitotic cells stiffen through myosin activity. (*a*) Restoration of myosin activity during rheological sampling of a mitotic cell treated with blebbistatin (2.5 μM). At time $\approx$180 s, the cell is exposed to blue light for an exposure time of $\approx$10 s (*gray area*), which causes a photoinactivation of blebbistatin (myosin II inhibitor) and thereby restores myosin II activity. This leads to a drastic force increase together with an increase of the force oscillation amplitude. Due to active blebbistatin slowly reentering the cell, average force and oscillation amplitude gradually decrease again over a timescale of $\approx$10 min. (*b*) Magnitude of 2D complex elastic modulus in dependence upon momentary cell surface tension measured during the interval of gradual force decrease. Values were averaged over several cells ($f = 1$ Hz, $N = 7$ and $f = 0.1$ Hz, $N = 8$). Error bars represent SDs. (*c* and *d*) Rheological parameters K_h and τ_{max}, dependent upon cell surface tension. Parameters were obtained by fitting averaged values of storage and loss moduli measured at different, binned values of cell surface tension. Error bars are SDs of fit parameters as obtained from bootstrapping using Gaussian random variates ($N = 30$). Measurements were carried out with detached cells on PEG-coated dishes to avoid potential cell shape changes upon varying cell surface tension. To see this figure in color, go online.

parameter values K_h and τ_{max} as a function of cell surface tension γ_{st}. While K_h increases roughly linearly for increasing γ_{st}, the cutoff timescale τ_{max} decreases (Fig. 6, *c* and *d*).

To investigate the possible influence of microtubules in the system, we studied the effect of taxol, which stabilizes microtubules and nocodazol, which depolymerizes them. In the presence of either drug, the cell surface tension is slightly increased, suggesting that the activity of myosin is enhanced in the absence of dynamic microtubules consistent with earlier findings (9,24). Furthermore, addition of taxol (100 nM) tends to reduce values of storage and loss moduli at low frequencies while phase shifts increase. Correspondingly, τ_{max} is also reduced (Table 1, rows 2 and 3; Fig. S14).

We also examined the influence of the actin cross-linker α-actinin-4 (*ACTN4*) on cortical mechanics. Just like actin, α-actinin-4 is mainly localized to the cell cortex during mitosis (Fig. S6 *d*) (25). Knock-down of α-actinin-4 through RNA interference leads to a reduction of steady-state tension in both chemically arrested mitotic cells (Fig. S6, *a* and *b*) as well as in cells left to transition through mitosis (Fig. S6). A change of cortical architecture as a consequence of knock-down of α-actinin-4 is also reflected by a reduced cortical localization of myosin, and to a lesser extent of actin (Fig. S6 *c*). Oscillatory measurements of *ACTN4* knock-down cells show that storage and loss moduli are reduced while phase shifts increase. This indicates a fluidization of the cortex due to α-actinin-4 knock-down. Correspondingly, estimated values of τ_{max} and K_h are reduced as compared to control cells (Table 1, row 5; Fig. S13).

Finally, we studied cells in the presence of the actin-depolymerizing drug latrunculin A (200 nM) in combination with the myosin II inhibitor blebbistatin (10 μM). In this condition, we find strongly reduced storage and loss moduli, which is also reflected by a value of K_h that is reduced by approximately an order of magnitude. In addition, the characteristic timescale τ_{max} is reduced from $\approx$13 s in control cells to 4 s (Table 1, row 6; Fig. S14).

DISCUSSION

In this article, we have probed the mechanics of Hela cells and determined the 2D rheology of the cell cortex in mitotic arrest. To this end, we have performed dynamic uniaxial cell compression with a parallel plate assay. Parallel plate manipulation is an established method to probe cell mechanical properties of adherent interphase cells via microplates (26–28). We apply this method to mitotic cells using AFM. High cell surface tension in mitosis (10) together with AFM measurement precision allowed us to control cell shape accurately. Our measurements confirm earlier findings that the cortex dominates cell mechanics (Fig. 3) (10,29–33). Based on this finding, we determine the frequency-dependent storage and loss moduli of the 2D cell cortex using the dynamic force response of whole cells. Cortical tension arises as the combination of a time-independent active tension due to actomyosin contractility and a dynamic part characterized by a 2D time-dependent relaxation modulus (Eq. 1). We measure a corresponding storage modulus $G'_{2D} \approx 80$ mN/m for frequency $f = 1$ Hz, which is comparable to the area expansion moduli measured

Please cite this article in press as: Fischer-Friedrich et al., Rheology of the Active Cell Cortex in Mitosis, Biophysical Journal (2016), http://dx.doi.org/10.1016/j.bpj.2016.06.008

for MDCK II cells by AFM indentation (34) and approximately a factor-of-five smaller than area expansion moduli measured for preswollen red blood cells by micropipette aspiration (35). We can estimate a 3D shear elastic modulus $G^*_{3D}(\omega) = G^*_{2D}(\omega)/(2(1+\nu)d)$ of the cortical layer on the order of 100 kPa for $f = 1$ Hz, using $d \approx 200$ nm for the cortical thickness (36) and a Poisson ratio $\nu = 0.5$, corresponding to an incompressible material. Comparable moduli have been reported for actin-rich structures such as muscle fibers or actin stress fibers (37,38). We have also analyzed our data calculating effective 3D elastic moduli of the entire cell. We obtain a storage modulus of ~1300 kPa during mitotic arrest at $f = 1$ Hz . For interphase cells, we find $\approx$300 Pa (Fig. S8, *a* and *b*). These effective cell moduli are consistent with earlier measurements determining cell elasticity (20,21). Interestingly, this effective cell modulus is generated mainly by the rheology of the cell cortex, as we show in this work.

Our measurement of dynamic storage and loss moduli allow us to discuss frequency-dependent material properties of the cell cortex. At frequencies <0.02 Hz, the loss modulus dominates and the cortical response becomes fluidlike. This suggests that the cortex behaves like a viscous fluid at slow timescales. This emergence of fluidity might be due to the turnover of actin cross linkers and actin filaments, which leads to the relaxation of elastic stresses at long times (2). Because of this fluidlike behavior, the cortex flows in response to contractility gradients (39,40). Such cortical flows occur, for example, particularly during cell division, when the division is asymmetric, or during the formation of a contractile ring (39,41).

Our data suggest the existence of a longest relaxation time τ_{max}, which might be related to cortex turnover. Indeed, a simple rheological model with a constant relaxation spectrum and a cutoff timescale τ_{max} fits the rheological data well (Fig. 5). We compared this fit to fits of a Maxwell model and of a power law. The Maxwell model with only a single relaxation time does not fit the data. The power law does not capture the maximal relaxation time that corresponds to cortical turnover. As a consequence, it provides a poorer fit as compared to our model. This can be seen most clearly when fit to the loss modulus data (Fig. 5 *c*). However, when using the power law to fit the data, we obtain an exponent $\approx$0.3, similar to reported values (42,43).

The actin network is organized by a large number of associated proteins. However, it has been difficult to distinguish the roles of these different proteins for rheological properties of the mitotic cell cortex. In our assay, knock-down of myosin II and α-actinin both reduce the magnitude of the elastic modulus of the cortical layer, as suggested by previous work (44–52). However, our oscillation experiments show that myosin II tends to fluidize the cortex, while α-actinin tends to solidify it. The solidifying role of α-actinin has been extensively studied in the in vitro actin networks and in vivo (46,47,51). In terms of our rheological model, α-actinin knock-down reduces the characteristic timescale τ_{max}, suggesting enhanced cortical turnover under this condition. This is consistent with the observation that α-actinin overexpression inhibits actin turnover during cell division (53). Previous studies have reported both a fluidization or a solidification of actin networks through myosin activity. Myosin II has been shown to fluidize non-cross-linked networks (54) while cross-linked actin networks were reported to solidify when myosin was added (50). Several in vivo measurements have suggested a solidifying role of myosin for adherent cells (45,55), but a fluidizing effect for suspended cells (20) and myoblasts (52). Here, we observed a solidification when myosin II is inhibited, suggesting that myosin activity in the cortex modulates rheological properties and increases fluidity. This resembles the observed fluidization of cellular material properties when exposed to large external prestress (43,56). We speculate that the fluidization by myosin in mitotic HeLa cells observed here could stem from enhanced actin turnover in the cortical layer resulting from increased active tension. This is supported by the observation that actin turnover is augmented by myosin activity during cytokinesis of mammalian cells (57).

Despite extensive theoretical work that suggests that the best way to think about the cortex is as an active thin film, it has been difficult to test these ideas in vivo. By introducing uniaxial compression of cells and complementing this with a simple rheological model, our work provides a characterization of the time-dependent mechanical properties of the mitotic cortex, confirming that it behaves like an active fluid film on longer timescales. Modulation of the properties of this film drives cell morphology and tissue reorganization.

SUPPORTING MATERIAL

Supporting Materials and Methods and 17 figures are available at http://www.biophysj.org/biophysj/supplemental/S0006-3495(16)30441-6.

AUTHOR CONTRIBUTIONS

E.F.-F. and C.J.C. performed research and analyzed the data; Y.T. contributed new reagents and analytic tools; E.F.-F., D.J.M., A.A.H., and F.J. designed the research; and E.F.-F., Y.T., C.J.C., D.J.M., A.A.H., and F.J. wrote the article.

ACKNOWLEDGMENTS

We thank Benjamin Friedrich, Guillaume Salbreux, Alexander Mietke, Louise Jawerth, and Stefan Münster for helpful discussions on cell mechanics and Jochen Guck and Moritz Kreysing for kind access to Comsol Multiphysics software. Furthermore, we thank Martin Stewart for advice on trans-mitotic AFM measurements and discussions about the consequences of impaired cortex integrity, Subramanian Ramanathan and Jonne Helenius for advice on quantification of cortical components, and the E. Paluch laboratory for contributing the Lifeact-mCherry expressing HeLa cell line.

This work was supported by the Eidgenössische Technische Hochschule Zürich (research grant No. ETH-05 11-2).

REFERENCES

1. Lecuit, T., and P.-F. Lenne. 2007. Cell surface mechanics and the control of cell shape, tissue patterns and morphogenesis. *Nat. Rev. Mol. Cell Biol.* 8:633–644.
2. Salbreux, G., G. Charras, and E. Paluch. 2012. Actin cortex mechanics and cellular morphogenesis. *Trends Cell Biol.* 22:536–545.
3. Hyman, A. A., C. A. Weber, and F. Jülicher. 2014. Liquid-liquid phase separation in biology. *Annu. Rev. Cell Dev. Biol.* 30:39–58.
4. Fehon, R. G., A. I. McClatchey, and A. Bretscher. 2010. Organizing the cell cortex: the role of ERM proteins. *Nat. Rev. Mol. Cell Biol.* 11:276–287.
5. Umetsu, D., B. Aigouy, …, C. Dahmann. 2014. Local increases in mechanical tension shape compartment boundaries by biasing cell intercalations. *Curr. Biol.* 24:1798–1805.
6. Rauzi, M., P. Verant, …, P.-F. Lenne. 2008. Nature and anisotropy of cortical forces orienting *Drosophila* tissue morphogenesis. *Nat. Cell Biol.* 10:1401–1410.
7. Eisenhoffer, G. T., P. D. Loftus, …, J. Rosenblatt. 2012. Crowding induces live cell extrusion to maintain homeostatic cell numbers in epithelia. *Nature.* 484:546–549.
8. Théry, M., A. Jiménez-Dalmaroni, …, F. Jülicher. 2007. Experimental and theoretical study of mitotic spindle orientation. *Nature.* 447:493–496.
9. Stewart, M. P., J. Helenius, …, A. A. Hyman. 2011. Hydrostatic pressure and the actomyosin cortex drive mitotic cell rounding. *Nature.* 469:226–230.
10. Fischer-Friedrich, E., A. A. Hyman, …, J. Helenius. 2014. Quantification of surface tension and internal pressure generated by single mitotic cells. *Sci. Rep.* 4:6213.
11. Ramanathan, S. P., J. Helenius, …, D. J. Müller. 2015. Cdk1-dependent mitotic enrichment of cortical myosin II promotes cell rounding against confinement. *Nat. Cell Biol.* 17:148–159.
12. Stewart, M. P., A. W. Hodel, …, J. Helenius. 2013. Wedged AFM-cantilevers for parallel plate cell mechanics. *Methods.* 60:186–194.
13. Schubert, R., N. Strohmeyer, …, D. J. Müller. 2014. Assay for characterizing the recovery of vertebrate cells for adhesion measurements by single-cell force spectroscopy. *FEBS Lett.* 588:3639–3648.
14. Skoufias, D. A., S. DeBonis, …, F. Kozielski. 2006. S-trityl-L-cysteine is a reversible, tight binding inhibitor of the human kinesin Eg5 that specifically blocks mitotic progression. *J. Biol. Chem.* 281:17559–17569.
15. Puech, P.-H., K. Poole, …, D. J. Müller. 2006. A new technical approach to quantify cell-cell adhesion forces by AFM. *Ultramicroscopy.* 106:637–644.
16. Yoneda, M. 1964. Tension at the surface of sea-urchin egg: a critical examination of Cole's experiment. *J. Exp. Biol.* 41:893–906.
17. Clark, A. G. 2013. Thickness, Dynamics and Mechanics of the Actomyosin Cortex. Ph.D. thesis. Technische Universitaet Dresden, Dresden, Germany.
18. Phan-Thien, N. 2012. Understanding Viscoelasticity: An Introduction to Rheology. Springer Science & Business Media, Berlin, Germany.
19. Kunda, P., A. E. Pelling, …, B. Baum. 2008. Moesin controls cortical rigidity, cell rounding, and spindle morphogenesis during mitosis. *Curr. Biol.* 18:91–101.
20. Chan, C. J., A. E. Ekpenyong, …, F. Lautenschläger. 2015. Myosin II activity softens cells in suspension. *Biophys. J.* 108:1856–1869.
21. Rosenbluth, M. J., W. A. Lam, and D. A. Fletcher. 2006. Force microscopy of nonadherent cells: a comparison of leukemia cell deformability. *Biophys. J.* 90:2994–3003.
22. Straight, A. F., A. Cheung, …, T. J. Mitchison. 2003. Dissecting temporal and spatial control of cytokinesis with a myosin II inhibitor. *Science.* 299:1743–1747.
23. Sakamoto, T., J. Limouze, …, J. R. Sellers. 2005. Blebbistatin, a myosin II inhibitor, is photoinactivated by blue light. *Biochemistry.* 44:584–588.
24. Mandato, C. A., H. A. Benink, and W. M. Bement. 2000. Microtubule-actomyosin interactions in cortical flow and cytokinesis. *Cell Motil. Cytoskeleton.* 45:87–92.
25. Hutchins, J. R., Y. Toyoda, …, J. M. Peters. 2010. Systematic analysis of human protein complexes identifies chromosome segregation proteins. *Science.* 328:593–599.
26. Thoumine, O., and A. Ott. 1997. Time scale dependent viscoelastic and contractile regimes in fibroblasts probed by microplate manipulation. *J. Cell Sci.* 110:2109–2116.
27. Desprat, N., A. Richert, …, A. Asnacios. 2005. Creep function of a single living cell. *Biophys. J.* 88:2224–2233.
28. Fernández, P., P. A. Pullarkat, and A. Ott. 2006. A master relation defines the nonlinear viscoelasticity of single fibroblasts. *Biophys. J.* 90:3796–3805.
29. Ananthakrishnan, R., J. Guck, …, J. Käs. 2006. Quantifying the contribution of actin networks to the elastic strength of fibroblasts. *J. Theor. Biol.* 242:502–516.
30. Yeung, A., and E. Evans. 1989. Cortical shell-liquid core model for passive flow of liquid-like spherical cells into micropipets. *Biophys. J.* 56:139–149.
31. Hochmuth, R. M. 2000. Micropipette aspiration of living cells. *J. Biomech.* 33:15–22.
32. Monteiro, E., J. Yvonnet, …, A. Asnacios. 2011. Analyzing the interplay between single cell rheology and force generation through large deformation finite element models. *Biomech. Model. Mechanobiol.* 10:813–830.
33. Nawaz, S., P. Sánchez, …, I. A. Schaap. 2012. Cell visco-elasticity measured with AFM and optical trapping at sub-micrometer deformations. *PLoS One.* 7:e45297.
34. Pietuch, A., B. R. Brückner, …, A. Janshoff. 2013. Elastic properties of cells in the context of confluent cell monolayers: impact of tension and surface area regulation. *Soft Matter.* 9:11490.
35. Evans, E. A., R. Waugh, and L. Melnik. 1976. Elastic area compressibility modulus of red cell membrane. *Biophys. J.* 16:585–595.
36. Clark, A. G., K. Dierkes, and E. K. Paluch. 2013. Monitoring actin cortex thickness in live cells. *Biophys. J.* 105:570–580.
37. Ogneva, I. V., D. V. Lebedev, and B. S. Shenkman. 2010. Transversal stiffness and Young's modulus of single fibers from rat soleus muscle probed by atomic force microscopy. *Biophys. J.* 98:418–424.
38. Hofmann, U. G., C. Rotsch, …, M. Radmacher. 1997. Investigating the cytoskeleton of chicken cardiocytes with the atomic force microscope. *J. Struct. Biol.* 119:84–91.
39. Mayer, M., M. Depken, …, S. W. Grill. 2010. Anisotropies in cortical tension reveal the physical basis of polarizing cortical flows. *Nature.* 467:617–621.
40. Salbreux, G., J. Prost, and J. F. Joanny. 2009. Hydrodynamics of cellular cortical flows and the formation of contractile rings. *Phys. Rev. Lett.* 103:058102.
41. Cao, L. G., and Y. L. Wang. 1990. Mechanism of the formation of contractile ring in dividing cultured animal cells. II. Cortical movement of microinjected actin filaments. *J. Cell Biol.* 111:1905–1911.
42. Pullarkat, P. A., P. A. Fernández, and A. Ott. 2007. Rheological properties of the eukaryotic cell cytoskeleton. *Phys. Rep.* 449:29–53.
43. Kollmansberger, P., C. T. Mierke, and B. Fabry. 2011. Nonlinear viscoelasticity of adherent cells is controlled by cytoskeletal tension. *Soft Matter.* 7:3127.
44. Wang, N., I. M. Tolić-Nørrelykke, …, D. Stamenović. 2002. Cell prestress. I. Stiffness and prestress are closely associated in adherent contractile cells. *Am. J. Physiol. Cell Physiol.* 282:C606–C616.

Please cite this article in press as: Fischer-Friedrich et al., Rheology of the Active Cell Cortex in Mitosis, Biophysical Journal (2016), http://dx.doi.org/10.1016/j.bpj.2016.06.008

45. Stamenović, D., B. Suki, …, J. J. Fredberg. 2004. Rheology of airway smooth muscle cells is associated with cytoskeletal contractile stress. *J. Appl. Physiol.* 96:1600–1605.

46. Tseng, Y., and D. Wirtz. 2001. Mechanics and multiple-particle tracking microheterogeneity of α-actinin-cross-linked actin filament networks. *Biophys. J.* 81:1643–1656.

47. Tseng, Y., T. P. Kole, and D. Wirtz. 2002. Micromechanical mapping of live cells by multiple-particle-tracking microrheology. *Biophys. J.* 83:3162–3176.

48. Sen, S., M. Dong, and S. Kumar. 2009. Isoform-specific contributions of α-actinin to glioma cell mechanobiology. *PLoS One.* 4:e8427.

49. Gardel, M. L., J. H. Shin, …, D. A. Weitz. 2004. Elastic behavior of cross-linked and bundled actin networks. *Science.* 304:1301–1305.

50. Koenderink, G. H., Z. Dogic, …, D. A. Weitz. 2009. An active biopolymer network controlled by molecular motors. *Proc. Natl. Acad. Sci. USA.* 106:15192–15197.

51. Ward, S. M. V., A. Weins, …, D. A. Weitz. 2008. Dynamic viscoelasticity of actin cross-linked with wild-type and disease-causing mutant α-actinin-4. *Biophys. J.* 95:4915–4923.

52. Balland, M., A. Richert, and F. Gallet. 2005. The dissipative contribution of myosin II in the cytoskeleton dynamics of myoblasts. *Eur. Biophys. J.* 34:255–261.

53. Mukhina, S., Y. L. Wang, and M. Murata-Hori. 2007. α-actinin is required for tightly regulated remodeling of the actin cortical network during cytokinesis. *Dev. Cell.* 13:554–565.

54. Humphrey, D., C. Duggan, …, J. Käs. 2002. Active fluidization of polymer networks through molecular motors. *Nature.* 416:413–416.

55. Fabry, B., G. N. Maksym, …, J. J. Fredberg. 2001. Scaling the microrheology of living cells. *Phys. Rev. Lett.* 87:148102.

56. Bursac, P., G. Lenormand, …, J. J. Fredberg. 2005. Cytoskeletal remodelling and slow dynamics in the living cell. *Nat. Mater.* 4:557–561.

57. Murthy, K., and P. Wadsworth. 2005. Myosin-II-dependent localization and dynamics of F-actin during cytokinesis. *Curr. Biol.* 15:724–731.

Biophysical Journal, Volume *111*

Supplemental Information

Rheology of the Active Cell Cortex in Mitosis

Elisabeth Fischer-Friedrich, Yusuke Toyoda, Cedric J. Cattin, Daniel J. Müller, Anthony A. Hyman, and Frank Jülicher

Supporting Material

Rheology of the active cell cortex in mitosis

E. Fischer-Friedrich,[1,2] Y. Toyoda,[1,3] C. J. Cattin,[4] D. J. Müller,[4] A. A. Hyman,[1] and F. Jülicher[2]

[1] *Max Planck Institute of Molecular Cell Biology and Genetics, Dresden, Germany*

[2] *Max Planck Institute for the Physics of Complex Systems, Dresden, Germany*

[3] *Institute of Life Science, Kurume University, Kurume, Japan*

[4] *Departement of Biosystems Science and Engineering, Eidgenössische Technische Hochschule Zürich, Basel, Switzerland*

I. ELASTIC MODULI OF A SIMPLE RHEOLOGICAL MODEL

In the following, we will derive the functional shape of the relaxation modulus and the complex elastic modulus for our simple rheological model introduced in the main text (Section "Rheology of the active cell cortex in mitosis"). This model relies on the assumption of a constant relaxation spectrum $h(\tau)$ up to a cut-off time scale τ_{max} after which the spectrum drops to zero (Fig. S1a). This simple form of the relaxation spectrum was derived as a simplified version of a reconstructed relaxation spectrum using measured rheological data (Fig. S1b) [1]. We define

$$h(\tau) = \begin{cases} K_h, & t < \tau_{max} \\ 0, & t \geq \tau_{max} \end{cases} \quad . \tag{S1}$$

Here, K_h is a stiffness that characterizes the spectrum amplitude and τ denotes the relaxation time variable. The relaxation modulus of a material with relaxation spectrum $h(\tau)$ is defined by the relation [2]

$$G(t) = \int_0^\infty h(\tau)\frac{\exp(-t/\tau)}{\tau}d\tau = \int_{-\infty}^\infty h(\tau)\exp(-t/\tau)\,d\ln(\tau) \quad , \tag{S2}$$

and the corresponding complex elastic modulus $G^*(\omega) = G'(\omega) + iG''(\omega)$ is given by

$$\begin{aligned} G'(\omega) &= \int_0^\infty \frac{\omega^2\tau}{(1+\omega^2\tau^2)}h(\tau)d\tau \\ G''(\omega) &= \int_0^\infty \frac{\omega}{(1+\omega^2\tau^2)}h(\tau)d\tau \quad . \end{aligned} \tag{S3}$$

Using Eq. (S2), a constant cut-off relaxation spectrum defined by Eq. (S1) gives rise to a relaxation modulus

$$G(t) = -K_h\mathrm{Ei}(-t/\tau_{\max}) \quad , \tag{S4}$$

where Ei denotes the exponential integral. Inserting the relaxation spectrum (S1) into Eqn. (S3), we find a storage and a loss modulus of the form

$$G'(\omega) = \frac{K_h}{2}\log(1+(\tau_{max}\omega)^2) \tag{S5}$$

$$G''(\omega) = K_h\arctan(\tau_{max}\omega) \quad . \tag{S6}$$

It is noteworthy that the storage modulus scales proportional to $\log(\omega)$ for large values of ω.

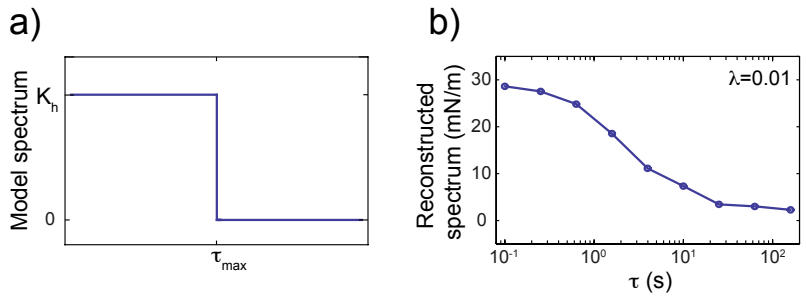

FIG. S1: Relaxation spectra of viscoelastic behavior. a) Relaxation spectrum of our rheological model. b) Relaxation spectrum reconstructed from rheological data presented in the main text (Section "Oscillatory forcing of the cell cortex"). The spectrum was calculated using Tikhonov regularization with regularization parameter $\lambda = 0.01$ [1].

For comparison, we will briefly discuss the functional shape of the relaxation spectrum $h(\tau)$, the relaxation modulus $G(t)$, and storage and loss modulus for the well-known Maxwell model and for a power law model. The Maxwell model exhibits a relaxation spectrum which is a delta peak $h(\tau) = k\delta(\tau - \tau_0)$. The associated relaxation modulus is the exponential decay $k\exp(-t/\tau_0)$ and storage and loss moduli can be calculated to be $k\omega^2\tau_0^2/(1+\omega^2\tau_0^2)$ and $k\omega\tau_0/(1+\omega^2\tau_0^2)$, respectively [2]. In the case of a power law rheology, the relaxation spectrum and the relaxation modulus are both a power law decay $\propto \tau^{-\beta}$, while storage and loss modulus are both proportional to ω^β [3].

II. DATA ANALYSIS OF STEPWISE UNIAXIAL CELL COMPRESSION

In the main text, we present experiments where cells in mitotic arrest were stepwise uniaxially compressed starting from different reference cell geometries at increasingly decreased cell heights. Each compression step was realized by a lowering of the cantilever by a distance Δh and accompanied by a force increase ΔF. In Fig. 3b, main text, and Fig. S11, we show the dependence of the force increase ΔF on normalized cell height reduction ξ in the reference state. To generate data depicted in Fig. 3b and Fig. S11, values of $\Delta F, \Delta h$ and normalized cell height reduction ξ were extracted for each compression step of a cell. In Fig. S11, values of $\Delta F/\Delta h$ were then plotted versus ξ. In Fig. 3b, data were normalized according to their estimated y-intercept and depicted in a log-linear plot.

Determination of $\Delta F, \Delta h$ and ξ. To probe cell stiffness at equal time scales, we extracted the force increase after a fixed compression time of 1 s (Note that the time span of the full compression step was partly longer ranging from $\approx 1-2$ s.). As we used a compression speed of $0.5\,\mu$m/s, a compression time of 1 s corresponds to a displacement of the AFM piezo by $0.5\,\mu$m. We will denote the cantilever height and the measured force after 1 s of compression by h_{1s} and F_{1s}, respectively. The height decrement Δh is calculated as $(h_{bef} - h_{1s})$, where h_{bef} denotes the cantilever height in steady state before the compression step. The value of Δh is generally smaller than the piezo deflection of $0.5\,\mu$m due to an increasing cantilever deflection. The corresponding force increase ΔF is estimated as $\Delta F = F_{1s} - F_{st,1s}$, where $F_{st,1s}$ is the steady state force corresponding to the cantilever height h_{1s}. This steady state force $F_{st,1s}$ was estimated as linear interpolation between steady state forces before ($F_{st,bef}$) and after ($F_{st,aft}$) the compression step. Therefore,

$$F_{st,1s} = F_{st,bef} + \frac{(h_{bef} - h_{1s})}{(h_{bef} - h_{aft})}(F_{st,aft} - F_{st,bef}) \quad ,$$

where h_{bef} and h_{aft} denote the cantilever height in steady state before and after the compression step, respectively. We experimentally verified that this is a very good approximation of steady state force for compression steps of $0.5-1\,\mu$m ($\lesssim 5\%$ error). To associate a value of ξ to a compression step, we calculated $\xi = 1 - 0.5(h_{bef})/(2R)$ which represents the cell height reduction before a compression step.

III. ANALOGY BETWEEN ELASTIC AND VISCOELASTIC DEFORMATIONS

In the main text, we were motivating the mechanical dominance of the cell cortex by comparing our experimental measurements of cell compression with theoretical calculations of uniaxial compres-

sion of elastic model cells (Fig. 3, main text). To motivate why the insight obtained from elastic deformations (Fig. 2, main text) applies to a viscoelastic object like a cell, we infer an analogy between the elastic and viscoelastic case. If a constant strain rate $\Delta\epsilon/\Delta t$ is applied to a stress-free, viscoelastic object in the time interval $[0, \Delta t]$, the peak stress at the end of this interval equals $\langle G(t)\rangle_{\Delta t}\Delta\epsilon$, where $\langle G(t)\rangle_{\Delta t}$ denotes the time average of the relaxation modulus in the interval $[0, \Delta t]$. Hence, provided a constant strain rate and a fixed time interval Δt of strain application, there is a stress-strain relation for the peak stress $\sigma(\Delta t)$ analogous to Hook's law with effective elastic constant $\langle G(t)\rangle_{\Delta t}$. This relation provides a quantitative analogy to the elastic case. In more simple terms one may say that an effective elastic constant $\langle G(t)\rangle_{\Delta t}$ may be associated to the viscoelastic system if a fixed range of time scales $[0, \Delta t]$ is probed.

IV. OSCILLATORY CELL FORCING AND DETERMINATION OF THE TWO-DIMENSIONAL ELASTIC MODULUS

Implementation of sinusoidal AFM cantilever motion. To implement cantilever motions for oscillatory cell compressions, we first approximated the sin-function as a piecewise-linear function (Fig. S2). To do this, we used four linear segments in the interval $[0, \pi/2]$, whose end points were optimized in terms of a least squares fit to match the sin-function most closely. The piecewise-linear function was then extended to the interval $[0, 2\pi]$ according to the symmetries of the sin-function. Oscillatory cantilever motions were then realized through an accordant piecewise-linear function (frequency- and amplitude-adapted) in terms of cantilever height ramps which were programed in a force script in the JPK AFM software. This force script was then carried out in the "repeat infinitely" mode at the desired average cantilever height.

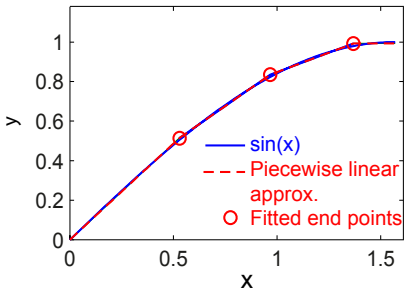

FIG. S2: Piecewise-linear approximation of sin function optimized by a least squares fit.

Cell height and cantilever oscillations are in phase. During oscillatory cell forcing, cantilever height oscillations alternate phases where the cantilever is pushed downwards with phases where the cantilever is lifted upwards. In phases of downwards movement, the cell height is forced to adapt immediately given a sufficiently stiff AFM cantilever. When the cantilever rises in the course of the oscillations, the cell follows the cantilever by increasing its height-extension since cellular surface tension drives it towards a round shape. This process of cell height relaxation may introduce a delay between cantilever height oscillations and cell height oscillations. We estimate the time scale of this delay as $\tau_{relax} \approx \frac{\eta_{cyt}}{p}\epsilon_{cyt}$ where η_{cyt} is the cytoplasmic viscosity, ϵ_{cyt} is a characteristic cytoplasmic bulk strain and p is the intracellular pressure excess. Intracellular cytoplasmic viscosity has been estimated in the range of $1 - 50\,\mathrm{Pa\,s}$ [4]. At a cantilever oscillation amplitude of $0.5\,\mu\mathrm{m}$ and an average cantilever height on the order of $10\,\mu\mathrm{m}$, a typical strain can be estimated as 0.05. Intracellular pressures measured are in the range of $100 - 500\,\mathrm{Pa}$ [5]. Therefore, the time scale τ_{relax} is expected to be $\leq 0.025\,\mathrm{s}$ which is an order of magnitude smaller than the smallest oscillation period sampled. We further checked whether measured phase shifts stay approximately constant if cantilever oscillation amplitudes (and thereby cytoplasmic strain and relaxation time) are reduced (Fig. S3). As this is indeed the case for the highest frequency measured ($f = 2\,\mathrm{Hz}$), we conclude that τ_{relax} is considerably smaller than $0.5\,\mathrm{s}$. We thus infer that cantilever height oscillations are to a good extent in phase with cellular height oscillations up to frequencies of $f = 2\,\mathrm{Hz}$.

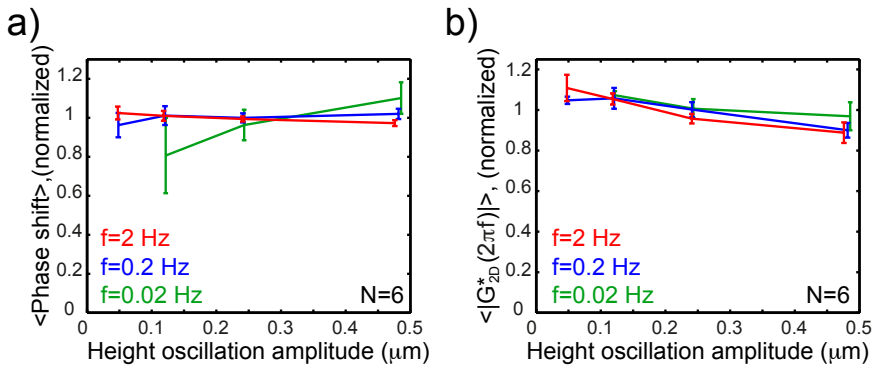

FIG. S3: Cell rheology in dependence of cantilever oscillation amplitude. a) Phase shift between stress and strain probed at cantilever oscillation amplitudes of 0.5 μm, 0.25 μm, 0.125 μm and 0.05 μm around a constant average cantilever height of $\approx$ 15 μm. At a given frequency, obtained phase shifts for different amplitudes were normalized by division through their mean value for each cell (N=6). Then the average of normalized amplitudes over six cells was calculated. For frequency $f = 0.02$ Hz, signal-to-noise ratios decreased (oscillations barely detectable) for declining oscillation amplitude giving rise to a large standard deviation and on average reduced phase shift. b) Same as in a but for magnitude of the estimated two-dimensional elastic modulus. Error bars show standard deviations. For $f = 0.02$ Hz, measurements at oscillation amplitudes of 0.125 μm and 0.05 μm gave too low signal-to-noise ratios and were therefore not considered.

Determining the two-dimensional complex elastic modulus. To determine the complex elastic modulus of cells from our measurements of oscillatory cell forcing, we determined a strain and an associated stress variable. As strain variable, we chose area strain of the total cell surface area. As associated stress variable, we calculated AFM force normalized to apparent tension $\gamma_{\mathrm{app}}(t)$. Defining stress and strain in that way, we could deduce a two-dimensional, complex elastic modulus from our oscillatory measurements defined as $G^*_{2D}(\omega) = \hat{\gamma}_{\mathrm{eff}}(\omega)/\hat{\epsilon}(\omega)e^{i\varphi(\omega)}$ where $\hat{\gamma}_{\mathrm{eff}}$ and $\hat{\epsilon}$ are estimated oscillation amplitudes of stress and strain, respectively, and φ is the phase shift between stress and strain.

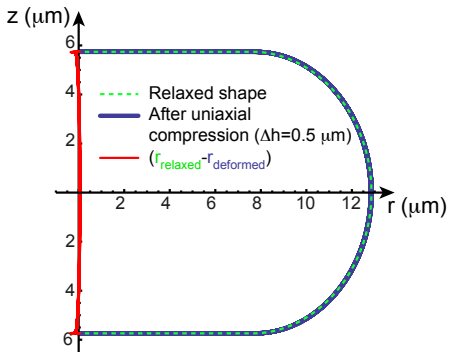

FIG. S4: Comparison of the steady state shapes of prestressed shells with and without elastic stresses due to uniaxial compression. Depicted are the profiles of the outer surface of an elastic shell in elastic equilibrium (dashed green) and of a shell with equilibrium height of 12 μm after a step of uniaxial compression by $\Delta h = 0.5\,\mu$m (dark blue). Shells have assigned an isotropic, in-plane prestress of 5000 Pa at a shell thickness of 200 nm and a total volume of 5000 μm^3. The shell height is set to 11.5 μm in both cases.

Data analysis of oscillatory measurements. In the following, we will describe how data from oscillatory cell compressions are analyzed in order to calculate stress and strain variables. For a cell measurement, we obtained the AFM cantilever height $h(t)$ and AFM force $F(t)$. From concurrent cell imaging, we could estimate a cellular volume V which was anticipated to stay constant during the measurement (Materials and Methods, main text). For every time point during the oscillation, cell surface area $A(t)$, cell curvature $H(t)$ and cell contact area with the compressing plates $A_{\mathrm{con}}(t)$ were estimated. To do this, we anticipated a shape of minimal surface area given the estimated cellular volume and the cantilever height $h(t)$ [5]. In steady state, we could show that this shape is a very good approximation of cell shape in mitosis due to present surface tension (deviations of less than 300 nm [5]). Calculations of the uniaxial compression of a (prestressed) elastic shell indicate that the shape after a compression step of $\Delta h = 0.5\,\mu$m is still very close to the shape of minimal surface area ($\leq 0.1\%$ deviation in surface area, Fig. S4). Using the assumption of a cell shape of minimal surface area, apparent tension $\gamma_{\mathrm{eff}}(t) = F(t)/(A_{\mathrm{con}}(t)2H(t))$ and surface area strain $\frac{A(t)}{\langle A\rangle}$ were calculated. Here, $\langle A\rangle$ denotes average surface area during oscillations.

We determined amplitudes and phase angles for calculated oscillatory signals of stress $\gamma_{\mathrm{eff}}(t)$ and strain $\frac{A(t)}{\langle A\rangle}$; for frequencies larger or equal to 1 Hz, typically ten and more oscillation periods were recorded and amplitudes and phase angles where estimated in terms of the discrete Fourier transform using Matlab. The discrete Fourier transform of the respective signal was estimated as a complex series $\{f_i\}_{i=1}^{N}$ by the command *fft*. We determined the peak of the absolute values of

$\{f_i\}_{i=1}^N$ at the index i_p. The phase angle is then calculated as the argument φ_{i_p} of the complex number $f_{i_p} = |f_{i_p}| \exp(i\varphi_{i_p})$ while the amplitude A of the signal is calculated as the integral over the peak

$$A = 2 \left(\sum_{i=\max(2,i_p-10)}^{i_p+10} |f_i|^2 \right)^{1/2} .$$

For frequencies smaller than 1 Hz, typically less than ten oscillation periods were recorded such that an analysis in terms of a Fourier transform was not reliable. Therefore, oscillation amplitudes and phase angles where estimated by performing a linear fit using the fit function $A\cos(2\pi t/T) + B\sin(2\pi t/T) + Ct$ where T is the oscillation period of the imposed cantilever oscillations. The phase angle of the signal was then calculated as $\arctan(A/B)$ while the amplitude was calculated as $A^2 + B^2$. As a control, we verified that for frequencies of around 1 Hz this method and the "Fourier method" give very close results for phase shift and signal amplitude. For oscillations periods of 50 and 100 s, typically only few oscillation periods were recorded, giving rise to a significant error of the extracted phase shift for associated frequencies.

V. DETERMINING RHEOLOGICAL PARAMETERS K_h AND τ_{max} FROM EXPERIMENTAL DATA

Fitting of storage and loss moduli. Our simple rheological model predicts a complex elastic modulus given by Eq. (S5) and (S6). This functional shape is fit to measured elastic moduli and allows thereby to determine K_h and τ_{max} from measured values of $G^*(\omega)$ for each cell. Experimental data of frequency-dependent storage and loss moduli were fit jointly by Eq. (S5) and (S6) with a least squares fit.

Fitting of force/tension decays. The relaxation modulus given by Eq. (S4) predicts stress relaxation after application of a compression step. Fitting of theoretically predicted stress decays to experimentally measured decays of apparent tension after steps of uniaxial cell compression allows to determine K_h and τ_{max} in an alternative way. Theoretically predicted tension decays $\gamma(t)$ were fit to the decay of measured apparent tension after a compression step of a cell. In the following, we describe how the fit function $\gamma(t)$ was calculated; measurements of compression steps were performed at a time resolution of $\Delta t = 0.1$ s. We calculated the tension generated in the time interval $[t_i, t_i + \Delta t]$ as

$$\gamma_{t_i \to t_i + \Delta t}(t) = \int_{t_i}^{t_i+\Delta t} G_{2D}(t - t')\dot{\epsilon}(t')dt' \approx \dot{\epsilon}(t_i) \int_{t_i}^{t_i+\Delta t} G_{2D}(t - t')dt'$$

using that the strain rate is roughly constant in the interval $[t_0, t_0 + \Delta t]$. The strain rate $\dot{\epsilon}(t)$ was estimated as area strain rate $(A_{cell}(t+\Delta t) - A_{cell}(t))/(A_{cell}(t_0)\Delta t)$, where $A_{cell}(t)$ is the estimated total cell surface area at time t. The overall tension at time t is then calculated as

$$\gamma(t) = \sum_{i=0}^{i=N} \gamma_{t_i \to (t_i + \Delta t)}(t)$$

where $\{t_i = t_0 + i\Delta t\}_{i=0}^{N}$ are time points of measurement during the process of cell compression. Fitted force decays as shown in Fig. 1c, main text, were generated by fitting the corresponding tension decay and then transforming fitted tension into force by the relation $F(t) = \gamma_{\text{eff}}(t)(A_{\text{con}}(t)2H(t))$, where $A_{\text{con}}(t)$ denotes the cell contact area with the compressing plates and $H(t)$ denotes the estimated mean curvature of the free cell surface.

VI. DEPENDENCE OF ELASTIC MODULI ON NORMALIZED CELL HEIGHT REDUCTION

We find that measured elastic moduli are to some extent dependent on the degree of cell height reduction (Fig. S5). The magnitude of elastic moduli tends to decrease for increasing values of normalized cell height reduction ξ for untreated cells. We speculate that geometrical effects may in part account for the decline of $|G^*_{2D}(\omega)|$ in dependence of ξ as suggested by calculations of the uniaxial compression of an elastic shell. At different levels of cell height reduction, shell bending at the contact line of shell and compressing plates gives different relative contributions to the overall compression force (Fig. S5c). For increasingly oblate shells, the relative contribution of bending goes down and the calculated stiffness value approaches the value of the elastic area bulk modulus of the shell ($K_A = Ed/2/(1-\nu)$) for strong cell height reduction. Here, E denotes the Young's modulus, d the thickness and ν the Poisson ratio of the shell.

Secondly, the decrease of $|G^*_{2D}(\omega)|$ for increasing ξ might partly originate from enhanced blebbing. The extrusion of small blebs, as commonly seen in cells with high surface tension at large values of ξ, might lead to an overestimation of cortical area strain in our analysis and therefore to an underestimation of elastic moduli at larger values of ξ. This effect may account for a decreased downwards slope of $|G^*_{2D}(\omega)|$ in the case of blebbistatin-treated cells.

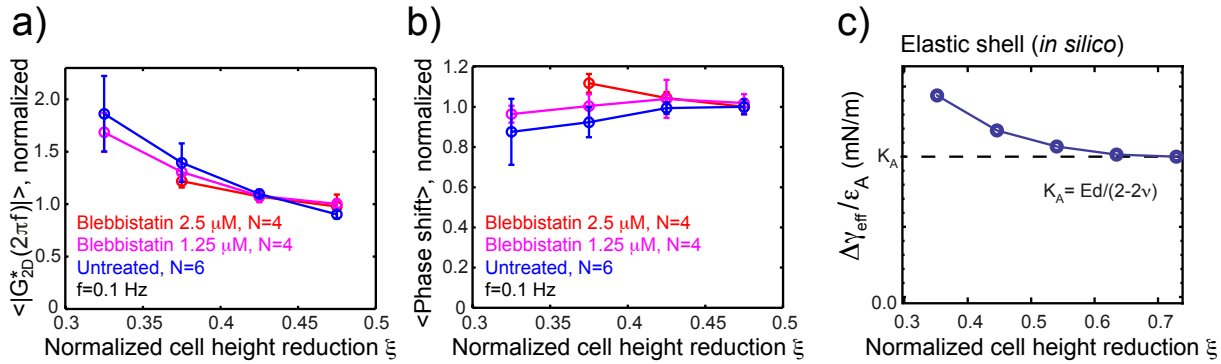

FIG. S5: Dependence of elastic moduli on the sampled degree of normalized cell height reduction. a) Magnitude of elastic modulus at $f = 0.1\,\mathrm{Hz}$ for untreated cells (blue, $N = 6$), cells treated with blebbistatin ($1.25\,\mu$M, magenta, $N = 4$ and $2.5\,\mu$M, red, $N = 4$). Each cell was sampled at different degrees of normalized cell height reduction at an oscillatory frequency of $0.1\,\mathrm{Hz}$ and an oscillation amplitude of $0.125\,\mu$m. Elastic moduli and phase shifts were calculated for each cell and normalized by division by their median value in the regime $\xi > 0.4$. Normalized data were then pooled and averaged over different cells. c) Stiffness values as obtained from finite element simulations of uniaxial compression of a prestressed, elastic shell (same parameters as in Fig. 2b, main text). Stiffness was calculated analogous to experimental measurements; the estimated increase of apparent tension $\Delta\gamma_{\mathrm{eff}}$ is divided by estimated area strain ϵ_A for the given deformation. For large ξ, stiffness converges to the value of the area bulk modulus $K_A = Ed/(2-2\nu)$, where d is the shell's thickness, and E and ν are the shell's Young's modulus and Poisson ratio, respectively ($E = 125\,\mathrm{kPa}$, $d = 200\,\mathrm{nm}$, $\nu = 0.49$).

VII. THE ACTIN CROSSLINKER α-ACTININ INFLUENCES TENSION AND ARCHITECTURE OF THE MITOTIC CORTEX

In mitotic cells, α-actinin-4 localizes strongly to the cell cortex (Fig. S6d). Knock-down of α-actinin-4 through RNA interference leads to a change of structural and mechanical properties of the mitotic cortex. In knock-down conditions, we find a reduction of cell surface tension (Fig. S6a,b) and a reduced fraction of cortical actin and myosin (Fig. S6c) as compared to control cells. In the course of mitosis, α-actinin-4 knock-down leads to a consistently reduced cell surface tension (Fig. S7). However, the duration of mitosis is not influenced by this tension drop (Fig. S7b).

Methods associated with Fig. S6 and S7: HeLa Kyoto cells expressing human H2B-GFP and mCherry-CAAX, human H2B-mCherry and human MYH9-GFP, human MYH9-GFP and Lifeact-mCherry or mouse ACTN4-GFP were cultured as described in the main text with additional $0.5\,\mu$g/ml Puromycin for cell lines with mCherry-tag (Life Technologies). RNA interference was performed as a forward transfection at a concentration of 10 nM with negative

controls (esiRNA: F-Luc, eupheria, HU-04832-1, siRNA: AllStars) and esiRNA or siRNA targeting ACTN4 (eupheria, HU-02773-1 or qiagen, Hs_ACTN4_5, SI02779973, target sequence: 5-acg cag cat cgt gga cta caa-3). Transfection was carried out using Lipofectamine RNAiMAX following the manufacturers instructions and assayed 48 hours post-transfection. For immunoblotting, primary antibodies were mouse monoclonal anti-ACTN4 (4D10, Sigma-Aldrich, USA) and rabbit monoclonal anti-GAPDH (14C10, Cell Signaling Technologies); secondary antibodies were HRP conjugated goat anti-rabbit (#170-6515, BioRad Laboratories, USA) and HRP conjugated goat anti-mouse (#170-6516, BioRad Laboratories). Cell surface tensions of cells in mitotic arrest were measured using the images acquired with an inverted light microscope (AxioObserver.Z1, Zeiss) and the cellular force response measured by a wedged cantilever mounted in the AFM head (CellHesion 200, JPK Instruments AG) (Fig. S7). Cells chemically arrested in prometaphase showing monopolar spindles were selected based on GFP fluorescence. The cantilever was lowered on the cell to a pre-set height and the resulting varying force was recorded over time. Once a steady plateau force value was reached, DIC and fluorescence images at the equatorial plane of the confined cell were recorded using a 20x air objective. All microscopy equipment was placed and experiments were carried out in a custom-made isolation box at 37°C (The Cube, Life Imaging Services, Switzerland). For experiments where cells were monitored during their passage through mitosis (Fig. S7), the experimental set-up consisted of an AFM (Cellhesion 200, JPK Instruments) mounted on an inverted confocal microscope (Observer.Z1, LSM 700, Zeiss). A 63x/1.3 LCI Plan-Neofluar water immersion objective (Zeiss) was used and images were recorded every 2 minutes. The cells were maintained at 37◦C using a Petri dish heater (JPK Instruments). AFM cantilevers used where modified to hold terminal wedges compensating for the intrinsic 10° tilt and produced as described before [6, 7].

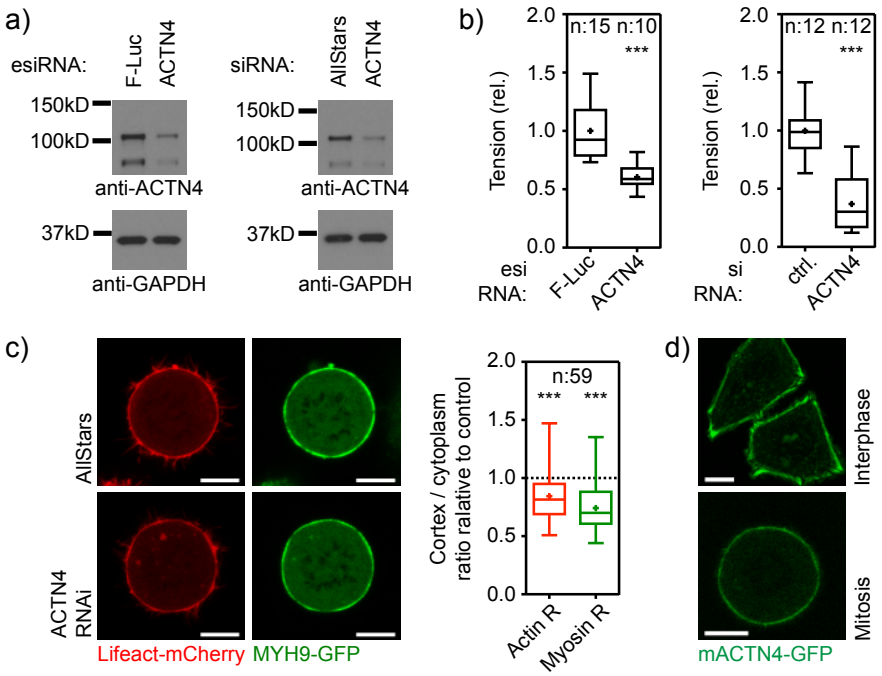

FIG. S6: RNAi-mediated depletion of α-actinin-4 results in decreased mitotic cell surface tension and altered cortical actin and myosin localization. a) Western blots of whole cell lysates of HeLa Kyoto cells expressing H2B-GFP and mCherry-CAAX, RNAi treated as indicated, using the antibodies indicated. b) Tension data of chemically arrested (2 μM S-Trityl-L-cysteine (STC)) mitotic HeLa Kyoto cells expressing H2B-GFP and mCherry-CAAX, RNAi treated with the constructs indicated, submitted to a height confinement assay. Values relative (rel.) to negative control average. ctrl., control cells c) Example images (left) and batch collected data (right) of chemically arrested (2 μM STC) mitotic HeLa Kyoto cells expressing MYH9-GFP and Lifeact-mCherry, RNAi treated with the constructs indicated, submitted to a height confinement assay. Values relative to negative control average. R, cortex/cytoplasm ratio of fluorescence intensity as detailed in Ramanathan *et al.* [8]. d) Example confocal micrograph of HeLa Kyoto cells expressing mACTN4-GFP with interphase- (top) and mitosis-specific (bottom) localization of mACTN4-GFP. Box, 25th to 75th percentile; Line, median; Whiskers, minimum to maximum; +, mean; n, number of cells characterized. Scale bar, 10 μm. Statistical significance was determined using the Mann-Whitney-test; ***, $p \leq 0.001$.

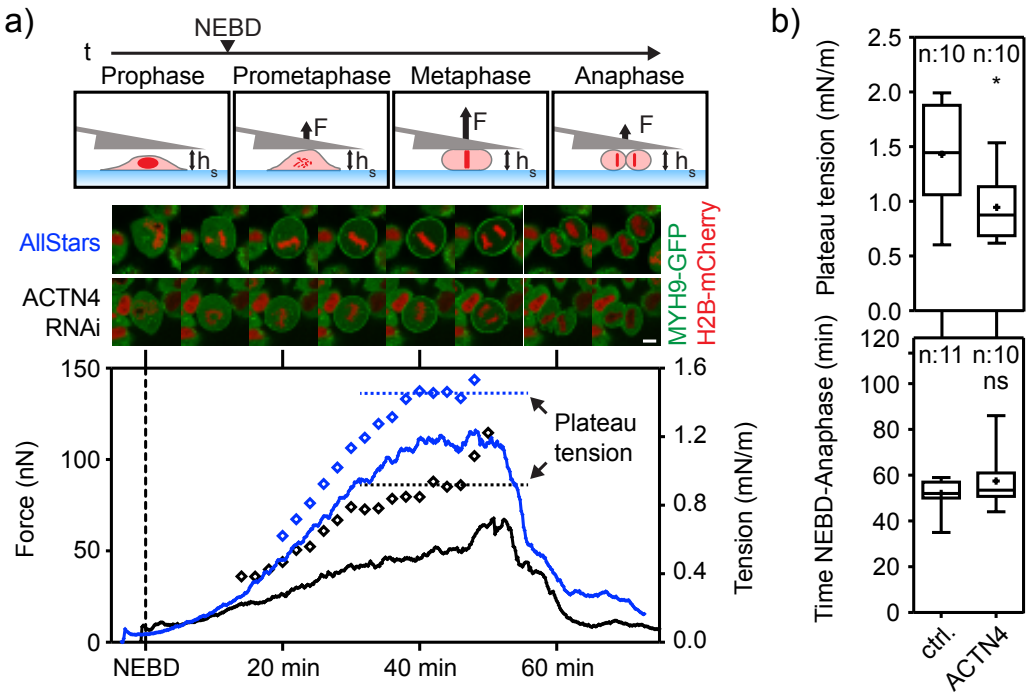

FIG. S7: RNAi-mediated depletion of α-actinin-4 results in decreased cell rounding tension trans-mitotically. a) Sketch (top), example force profiles (middle) and example confocal microscopy images (bottom) of HeLa Kyoto cells expressing H2B-mCherry and MYH9-GFP, RNAi treated with the constructs indicated, submitted to a trans-mitotic height confinement assay. Lines represent force traces and empty diamonds represent tension values. t, time; NEBD, nuclear envelope breakdown; F, force; h_s, set height. b) Plateau tension (top) and time from NEBD to anaphase onset (bottom) for cells analyzed as exemplified in a. Scale bar, 10 μm. Box, 25th to 75th percentile; Line, median; Whiskers, minimum to maximum; +, mean; n, number of cells characterized. Scale bar, 10 μm (all images). Statistical significance was determined using the Mann-Whitney-test; *, $p \leq 0.05$.

VIII. FINITE ELEMENT ELASTIC MODEL OF UNIAXIAL CELL COMPRESSION

Calculations were performed as finite element simulations in Comsol Multiphysics using the structural mechanics module. The program computed a stationary solution of an axisymmetric problem using linear elasticity theory. Before the deformation, the elastic model cell is set to be in its (elastic) equilibrium shape. Equilibrium shapes are chosen at different heights but identical cell volumes ($V = 5000\,\mu\mathrm{m}^3$).

The elastic model cell (shear-elastic bulk or shell) is sandwiched between two parallel, circular plates of high rigidity (E=200 GPa, ν =0.3) with a thickness of $1\,\mu$m. During a step of cell compression, both plates are moved towards each other by a defined distance $\Delta h/2$ (*prescribed displacement*). Contact between plates and model cell was defined through two *contact pairs* that included the upper (lower) boundary of the rectangle and the upper (lower) half of the model cell surface. By default, height decrements during cell compression were set to $\Delta h = 0.5\,\mu$m. Calculating height decrements Δh in between $0.1 - 1\,\mu$m yielded force increases scaling linearly with Δh.

Shear-elastic bulk. The first type of model cell was defined as an isotropic, elastic body. For simplicity, we defined its shape as a body of revolution generated by a rectangle and an adjacent semi-circle (black wire-frame in Fig. 2a, main text) with Young's modulus $E = 1000\,\mathrm{Pa}$ and Poisson ratio $\nu = 0.49$. The bulk volume was set to $5000\,\mu\mathrm{m}^3$. Mesh size was set as *user-controlled mesh* using the *general physics* option *finer*. The *free triangular* feature was used to refine the meshing associated to the bulk and the plate surface by setting the minimal element size to 0.05 μm. Again, with the *free triangular* option, the maximum element size in the bulk interior was set to 0.15 μm.

Elastic shell. The second type of model cell was defined as elastic shell of 200 nm thickness ($E = 125\,\mathrm{kPa}$ and Poisson ratio $\nu = 0.49$). The cell's shape was defined by the contour of a minimal surface area [5] with a total cell volume of $5000\,\mu\mathrm{m}^3$. The respective curve representing the free cell boundary is generated by Mathematica and then exported as a text file. This file is then imported into comsol as *interpolation curve*. The inner shell surface is defined from the outer surface subtracting the surface normal vector multiplied by the shell thickness. Furthermore, we assigned a uniform, constant mechanical prestress that mimics active tension in the cortex due to the presence of myosin motors. This is realized by assigning an *initial stress* to the shell domain by use of the structural mechanics module. The prestress is a constant, isotropic in-plane stress in the shell of magnitude σ_{act} (by default $5000\,\mathrm{Pa}$). In cylindrical coordinates (r, φ, z), the prestress

was assigned as

$$\begin{pmatrix} \sigma_{act} n_z^2 & 0 & -\sigma_{act} n_z n_r \\ 0 & \sigma_{act} & 0 \\ -\sigma_{act} n_z n_r & 0 & \sigma_{act} n_r^2 \end{pmatrix} \tag{S7}$$

where n_z and n_r are the component of the normal vector of the inner shell surface projected onto the z- and r-axis, respectively. For this definition of the stress, the normal vectors on the surface of the shell need to be referenced in the entire shell domain. To achieve this, we defined a *component coupling* operator of the type *general extrusion* with the source defined as inner shell boundary. At the inner boundary of the shell a *boundary load* in terms of a constant pressure is declared, that ensures conserved cell volume. The appropriate internal pressure was determined by repeatedly carrying out the simulation of uniaxial compression and determining resultant cell volume along with linear extrapolation of pressure values until a volume change of less than 0.02% was achieved. The shell mesh was defined as *user-controled mesh* using the *general physics* option *extra fine*. The *free triangular* feature was used to refine the meshing associated to the domain of the shell, the outer boundary of the shell and the surface of the disk-shaped plate that is in contact with the shell. The *maximum element size* inside the domain of the shell was set to 0.05 μm. The *maximum element size* of contacting plate surface was set to 0.1 μm. In addition, the *maximum element size* of the outer shell boundary was set to 0.05 or 0.025 μm, where the smaller value was used for shell heights of 6 and 8 μm, only.

In the case of the shell, ΔF as depicted in Fig. 3a,b, main text, is calculated as the force exerted on the plates after the compression step subtracted by the steady state force (due to prestress) at the new cell height.

IX. ALTERNATIVE ANALYSIS OF OSCILLATORY CELL FORCING

To compare our results with previous measurements that showed three-dimensional complex elastic moduli of cells, we also performed an alternative analysis of our data calculating effective three-dimensional Young's moduli. Using the most simple approach, we chose as stress variable $F(t)/\langle A_{eq}\rangle$ where $F(t)$ denotes time-dependent measured force, and $\langle A_{eq}\rangle$ denotes the average cross-sectional area at the cell equator. This geometrical parameter is directly obtained from cell imaging. We used $(\langle h\rangle - h(t))/\langle h\rangle$ as strain variable, where $h(t)$ denotes time-dependent cell height and $\langle h\rangle$ denotes its average. From this analysis, we obtain effective frequency-dependent cell elastic moduli in the range of $100 - 1500$ Pa for mitotic cells (Fig. S8a). For interphase cells, we

obtain values in the range $10 - 500$ Pa (Fig. S8b) which are comparable to effective cell elastic moduli reported earlier for rounded interphase cells [9, 10]. Note, that for this alternative analysis, storage and loss moduli derived from our model (Eqn. (4) and (5), main text) do not provide a good fit. A power law fit captures the calculated storage and loss moduli more closely. (We fitted $G'(\omega) = A\pi\omega^\beta \csc(\pi\beta/2)/2$ and $A\pi\omega^\beta \sec(\pi\beta/2)/2$ obtaining $A = 195\,\mathrm{Pa}$ ($68\,\mathrm{Pa}$) and $\beta = 0.2$ ($\beta = 0.24$) for mitotic cells (interphase cells).) However, in particular for mitotic cells (Fig. S8a), the loss modulus deviates from a power law behavior as it levels off at larger frequencies.

Interestingly, the effective 3D storage and loss moduli obtained in this alternative analysis look more similar to previously published data and show a different frequency dependence than the storage and loss moduli of the cortical layer discussed in Section 5, main text. The reason why the frequency dependence is different stems from the fact that the geometric factors used to define cortical 2D moduli are time-dependent. Time-dependent 2D cortical tension is defined as $\gamma_{\mathrm{eff}}(t) = F(t)/(A_{\mathrm{con}}(t)2H(t))$, where $A_{\mathrm{con}}(t)$ is the time-dependent contact area of the compressed cell and $H(t)$ is the mean curvature of the free cell surface. During oscillatory cell forcing, a periodic cell height change $h(t) = h_0 + \tilde{h}\exp(i\omega t)$ is imposed. Measured force and derived cortical tension oscillate accordingly as $F(t) = F_0 + \tilde{F}\exp(i\omega t)$ and $\gamma_{\mathrm{eff}}(t) = \gamma^0_{\mathrm{eff}} + \tilde{\gamma}_{\mathrm{eff}}\exp(i\omega t)$ and are in general phase-shifted with respect to cell height oscillations such that $\tilde{F}$ and $\tilde{\gamma}_{\mathrm{eff}}$ are complex numbers. To linear order, we have

$$F(t) = G_0\gamma^0_{\mathrm{eff}} + \left(\gamma^0_{\mathrm{eff}}\tilde{G} + G_0\tilde{\gamma}_{\mathrm{eff}}\right)\exp(i\omega t)\,,$$

where we have introduced a time-dependent geometric factor $G(t) = A_{\mathrm{con}}(t)2H(t)$ which oscillates periodically as $G(t) = G_0 + \tilde{G}\exp(i\omega t)$ in phase with height oscillations. Therefore,

$$\tilde{F} = \left(\gamma^0_{\mathrm{eff}}\tilde{G} + G_0\tilde{\gamma}_{\mathrm{eff}}\right).$$

Performing this analysis, we find that the real and imaginary part of $\tilde{F}$ and $\tilde{\gamma}_{\mathrm{eff}}$ are not proportional to each other due to the presence of the prestress γ^0_{eff}. Note that in passive systems, geometric changes usually enter to second order and therefore do not have such an effect. Thus the cell cortex with its actomyosin-induced active tension exhibits different rheological behavior when analyzed using the proper geometric factors as compared to a conventional interpretation where stress is essentially identified with force.

Finally, we also derived an effective, long-term 1D-stiffness of mitotic cells in Fig. S8c. This effective stiffness originates from a steady-state cell surface tension which mainly relies on active cortical tension in mitotic cells [5]. This stiffness was calculated from an increase of steady state force upon

stepwise cell height reduction (same data as in Fig. 3b, main text, each color codes for a single cell measured). Clearly, this effective stiffness increases for increasingly depressed cell heights. This trend is expected if measured steady state forces originate from a largely constant active cortical tension.

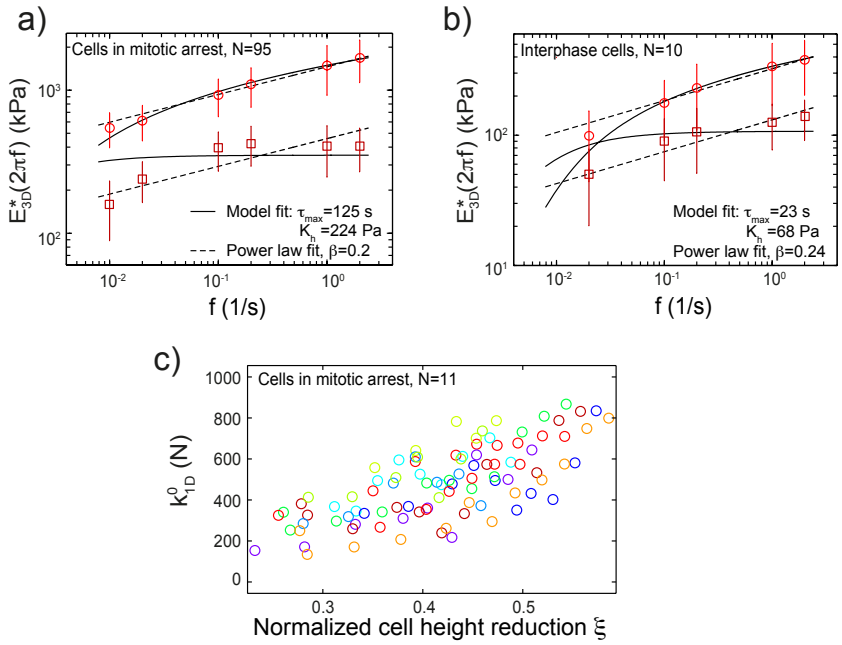

FIG. S8: Apparent dynamic Young's moduli of cells obtained from oscillatory cell forcing using a simple alternative data analysis. a) Effective dynamic Young's modulus of cells in mitotic arrest. b) Effective dynamic Young's modulus of cells in interphase. c) Effective 1D stiffness of mitotic cells derived from an increase of steady state force upon stepwise cell height reduction (same data as in Fig. 3b, main text, each color codes for a single cell measured). $k^0_{1D}(\xi) = \Delta F_{st}(\xi)/(\Delta h/2R)$ where $\Delta F_{st}(\xi)$ denotes the change in steady state force upon a compression step of Δh performed at a cell shape of normalized cell height reduction ξ. R denotes the cell radius associated to a spherical cell shape at constant cell volume.

[1] Honerkamp, P. J., and J. Weese, 1993. A nonlinear regularization method for the calculation of relaxation spectra. *Rheologica Acta* 32:65–73.

[2] Phan-Thien, N., 2012. Understanding Viscoelasticity: An Introduction to Rheology. Springer Science & Business Media.

[3] Kollmannsberger, P., and B. Fabry, 2011. Linear and Nonlinear Rheology of Living Cells. *Ann Rev Mater Res* 41:75–97.

[4] Wirtz, D., 2009. Particle-Tracking Microrheology of Living Cells: Principles and Applications. *Ann Rev Biophys* 38:301–326.

[5] Fischer-Friedrich, E., A. A. Hyman, F. Jülicher, D. J. Müller, and J. Helenius, 2014. Quantification of surface tension and internal pressure generated by single mitotic cells. *Sci Rep* 4:6213.

[6] Stewart, M. P., A. Hodel, A. Spielhofer, C. J. Cattin, D. J. Müller, and J. Helenius, 2013. Wedged AFM-cantilevers for parallel plate cell mechanics. *Methods* 59:186–194.

[7] Cattin, C. J., M. Düggelin, D. Martinez-Martin, C. Gerber, D. J. Müller, and M. P. Stewart, 2015. Mechanical control of mitotic progression in single animal cells. *PNAS* 112:11258–11263.

[8] Ramanathan, S. P., J. Helenius, M. P. Stewart, C. J. Cattin, A. A. Hyman, and D. J. Müller, 2015. Cdk1-dependent mitotic enrichment of cortical myosin II promotes cell rounding against confinement. *Nat Cell Biol* 17:148–159.

[9] Chan, C. J., A. E. Ekpenyong, S. Golfier, W. Li, K. J. Chalut, O. Otto, J. Elgeti, J. Guck, and F. Lautenschlger, 2015. Myosin II activity softens cells in suspension. *Biophys J* 108:1856–1869.

[10] Rosenbluth, M. J., W. A. Lam, and D. A. Fletcher, 2006. Force Microscopy of Nonadherent Cells: A Comparison of Leukemia Cell Deformability. *Biophys J* 90:2994–3003.

X. SUPPLEMENTARY FIGURES

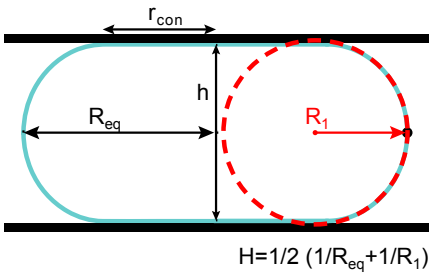

FIG. S9: Schematic of a cell confined between two parallel plates. During each measurement, the equatorial radius R_{eq} and the cell height h where measured. The mean curvature of the free cell surface area is calculated as $H = 0.5(1/R_1 + 1/R_{eq})$ using the two radii of principle curvatures in the equatorial plane. The principle curvature radius R_1 associated to the azimuthal direction is approximated as $R_1 \approx h/2$. Note that the mean curvature on the free cell surface is expected to be constant on the free cell surface due to Laplace's law [5]. The radius of contact r_{con} is the radius of the disk-shaped contact area with the plates.

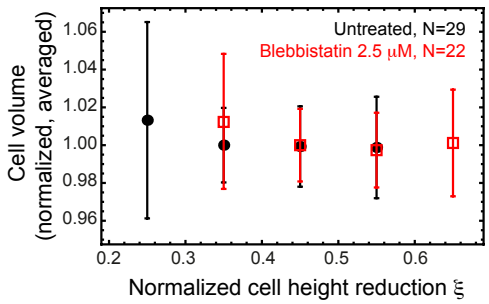

FIG. S10: Estimated cellular volume shows no trend of volume increase or decrease upon increasing uniaxial cellular compression (untreated: black, blebbistatin 2.5 μM: red). Cell volume was estimated for each level of height reduction using the cell's equatorial radius and assuming a shape of minimal surface area. Estimated volumes for one cell were normalized by division through its median volume. Error bars represent standard deviations.

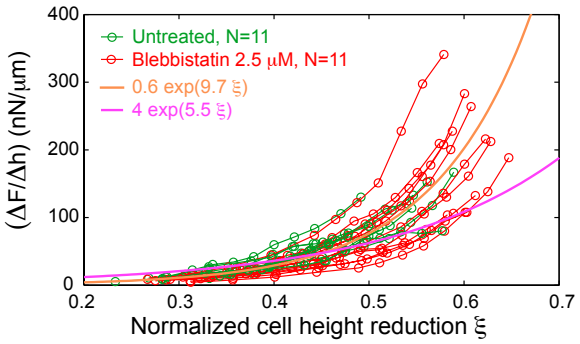

FIG. S11: Force increase after 1 s of uniaxial cell compression at constant speed. Connected data points correspond to the measurement of one cell at different degrees of cell height reduction ξ (untreated cells: green, N=11, blebbistatin-treated cells (2.5 μM): red, N=11). Orange and magenta lines indicate the trend of exponential functions with exponents of slope 5.5 and 9.7 which are expected for the scenario of a shear-elastic bulk or an elastic shell, respectively. Data are identical with those used in Fig. 3b, main text.

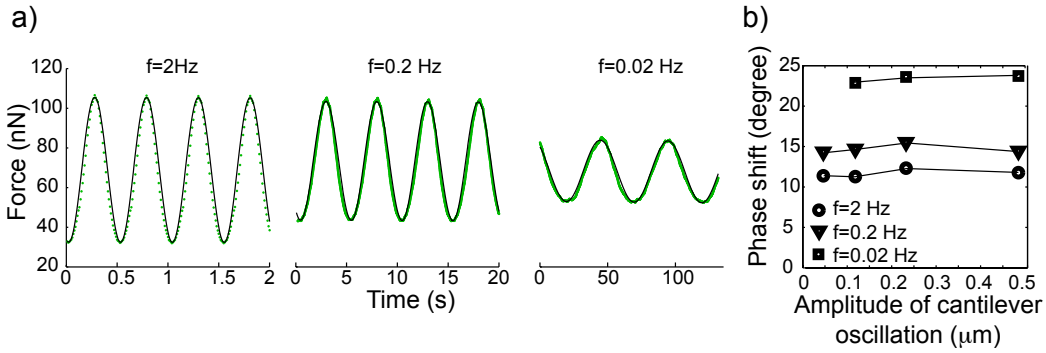

FIG. S12: Force oscillations are sinusoidal and scale linear with height amplitudes. a) Force oscillations are close to sinusoidal in shape in the measured frequency range (data: green dots, sinusoidal fit: black solid line). b) Measured phase shifts of oscillations are largely independent of the imposed oscillation amplitude of cell height up to height amplitudes of 0.5 μm . In Fig. 4c, main text, we show in addition that force amplitudes scale linearly with cell height amplitudes.

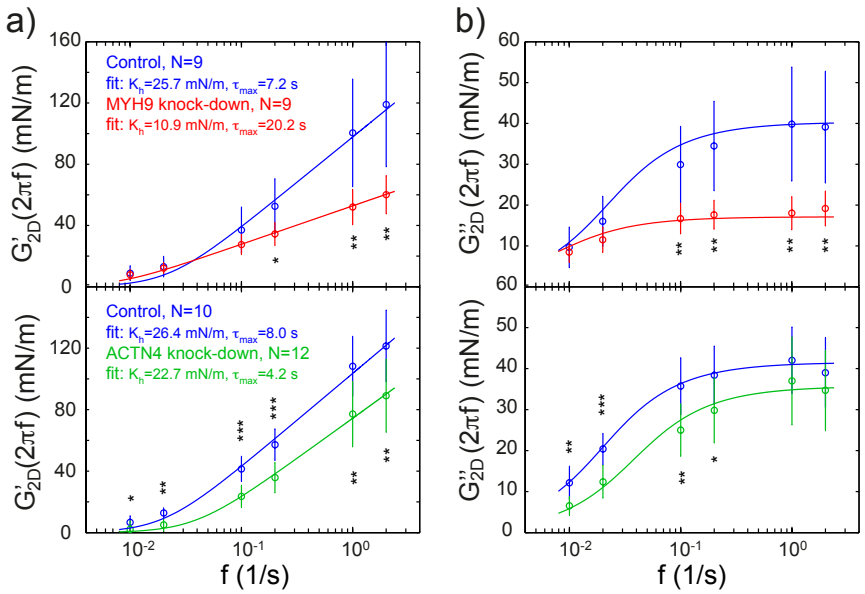

FIG. S13: Actin cross-linkers influence cortical rheology. Two-dimensional complex elastic moduli obtained from oscillatory sampling of cells after knock-down of myosin II and α-actinin-4 through RNA interference. Average storage modulus (a) and loss modulus (b) of control cells (blue) versus myosin II knock-down cells (red, top row) or α-actinin-4 knock-down cells (green, bottom row). Error bars indicate standard deviations. Associated fits of elastic moduli resultant from a constant, cut-off relaxation spectrum are indicated by solid lines. Statistical significance was determined using the Mann-Whitney-test; *, $p \leq 0.05$, **, $p \leq 0.01$, ***, $p \leq 0.001$.

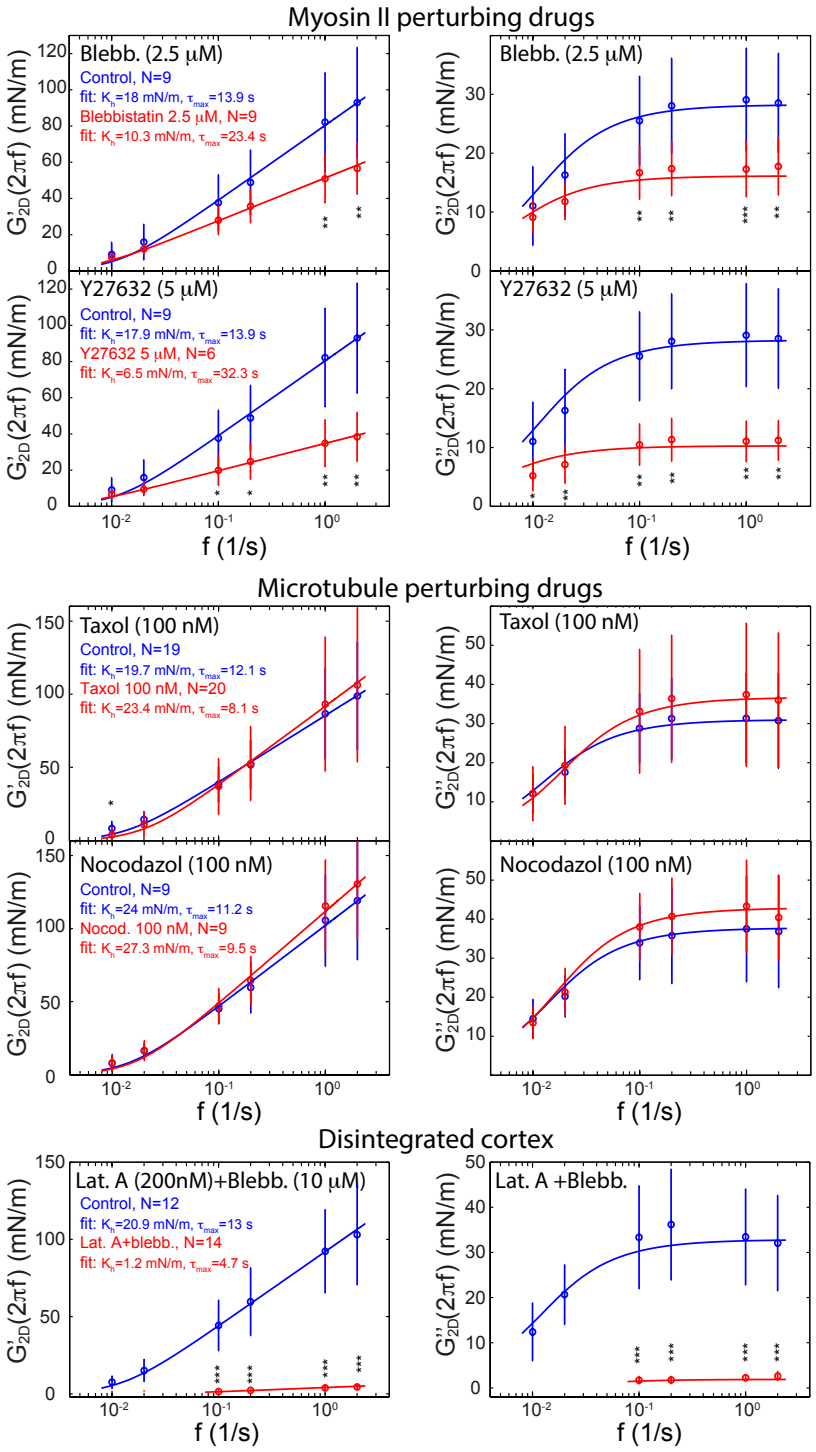

FIG. S14: Effect of cytoskeletal drugs on cortical rheology. Two-dimensional complex elastic modulus extracted from oscillatory sampling of cells after addition of cytoskeletal drugs as indicated (Materials and Methods). Average storage modulus (left) and loss modulus (right) of control cells (blue) versus drug-treated cells (red). Error bars indicate standard deviations. Fits of elastic moduli resultant from a constant, cut-off relaxation spectrum are indicated by solid lines. Statistical significance was determined using the Mann-Whitney-test; *, $p \leq 0.05$, **, $p \leq 0.01$, ***, $p \leq 0.001$. (Lat. A, latrunculin A, blebb., blebbistatin)

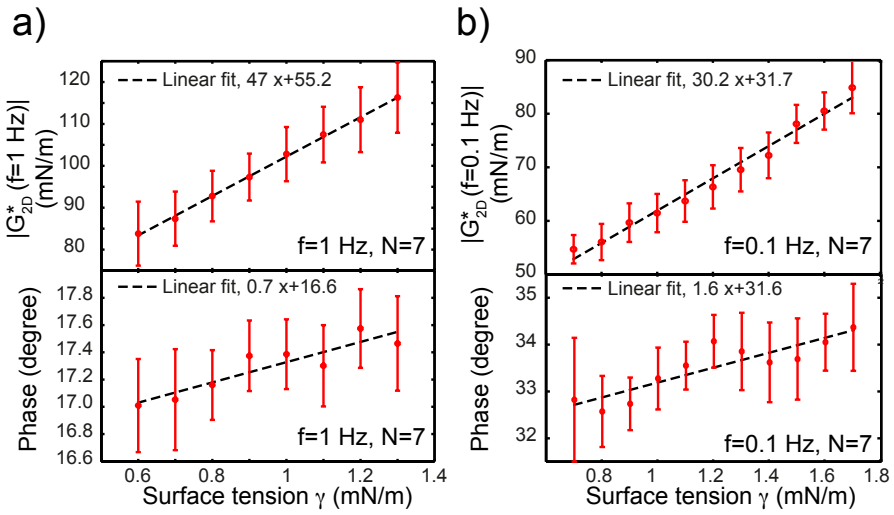

FIG. S15: Magnitude and phase of complex elastic modulus in dependence of changing surface tension as extracted from photo-inactivation experiments (Fig. 6, main text). Cells in mitotic arrest were treated with blebbistatin ($2.5-5\,\mu$M) and sampled via oscillatory cantilever height modulations. Upon exposure to blue light for $\approx$ 10s, average force and force amplitude increase. Due to active blebbistatin slowly reentering the cell, average force and oscillation amplitude gradually decrease down to their original values over a time period of $\approx$ 10min. In this time period, cell stiffness in dependence of varying cell surface tension was extracted. a,b) Averaged magnitude of elastic modulus (top row) and phase shift φ (bottom row) in dependence of estimated cell surface tension as derived from average force values for oscillation frequencies 1 Hz (a) and 0.1 Hz (b). Error bars show standard errors of the mean.

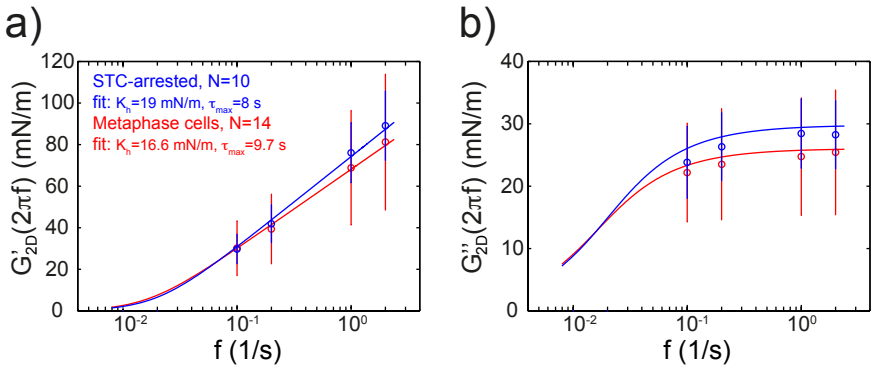

FIG. S16: Effect of mitotic arrest on cortical rheology. a,b) Two-dimensional complex elastic modulus extracted from oscillatory sampling of cells in mitotic arrest (2 μM S-Trityl-L-cysteine) or of cells in metaphase. Average storage modulus (left) and loss modulus (right) of arrested cells (blue) versus metaphase cells (red). Error bars indicate standard deviations. Fits of elastic moduli resultant from a constant, cut-off relaxation spectrum are indicated by solid lines. Cells in mitotic arrest on average show a slightly increased rheological parameter K_h ($\approx$ 14% higher, p-value: 0.04) while differences in the time scale τ_{max} are not statistically significant. Cells in mitotic arrest and in metaphase were measured at an average normalized cell height reduction of $\xi = 0.42$, both. We measured in a frequency range of $0.1 - 2$ Hz, as metaphase cells typically progressed to anaphase after ≈ 10 min and measurements of longer oscillation periods were thus not possible.

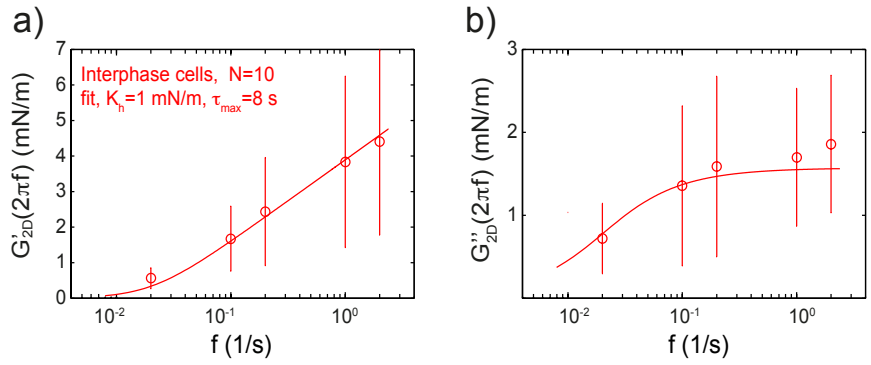

FIG. S17: Cell rheology in interphase. a,b) Two-dimensional complex elastic modulus extracted from oscillatory sampling of rounded interphase cells. Average storage modulus (left) and loss modulus (right) of interphase cells. Error bars indicate standard deviations. Fits of elastic moduli resultant from a constant, cut-off relaxation spectrum are indicated by solid lines. Cells were first detached from cell culture dishes with Trypsin/EDTA and measured on dishes coated with PLL-g-PEG (SuSoS) which prevents cell adhesion. Cells were measured at an average normalized cell height reduction of $\xi = 0.5$.